Cell Reports

Article

PGE_2-EP2/EP4 signaling elicits immunosuppression by driving the mregDC-Treg axis in inflammatory tumor microenvironment

Graphical abstract

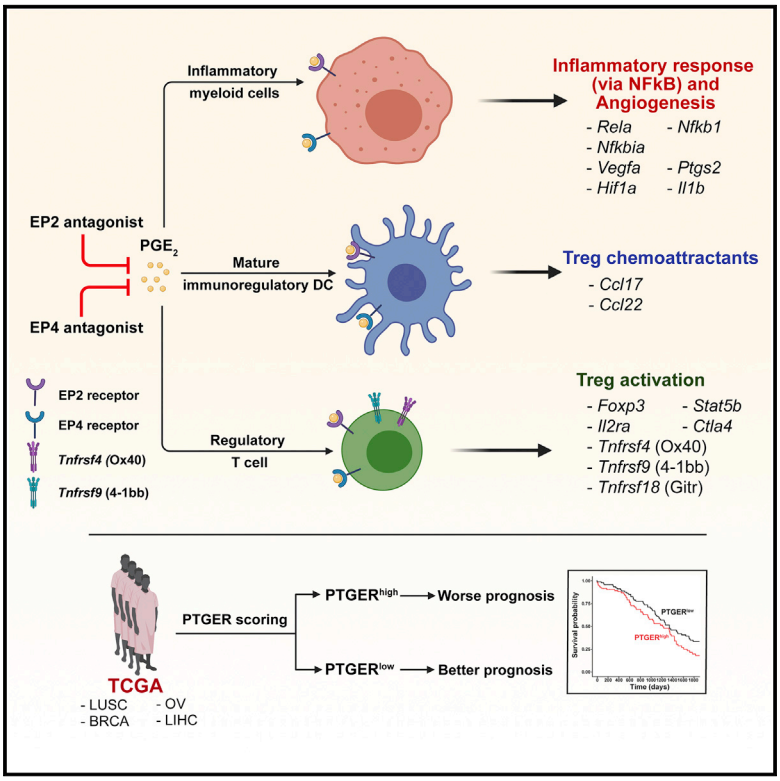

Highlights

- Antagonism of PGE receptors EP2 and EP4 suppresses LLC1 tumor growth in mice
- EP2/EP4 signaling boosts inflammation and angiogenesis through NF-κB in myeloid cells
- EP2/EP4 signaling elicits immunosuppression through Treg recruitment and activation
- EP2/EP4 expression level has prognosis value in various human cancers

Authors

Dean Thumkeo, Siwakorn Punyawatthananukool, Somsak Prasongtanakij, ..., Atsushi Tanaka, Shimon Sakaguchi, Shuh Narumiya

Correspondence

d.thumkeo@mfour.med.kyoto-u.ac.jp (D.T.), snaru@mfour.med.kyoto-u.ac.jp (S.N.)

In brief

Why active inflammation does not lead to immune activation in TME remains unclear. Thumkeo et al. have examined this issue in LLC1 mouse tumors and found that PGE_2-EP2/EP4 signaling functions as a regulatory node to control both inflammation and immunosuppression simultaneously in TME.

Thumkeo et al., 2022, Cell Reports *39*, 110914
June 7, 2022
https://doi.org/10.1016/j.celrep.2022.110914

Cell Reports

CellPress
OPEN ACCESS

Article

PGE_2-EP2/EP4 signaling elicits immunosuppression by driving the mregDC-Treg axis in inflammatory tumor microenvironment

Dean Thumkeo,[1,2,9,*] Siwakorn Punyawatthananukool,[1,9] Somsak Prasongtanakij,[1,10] Ryuma Matsuura,[1] Kentaro Arima,[1] Huan Nie,[1] Rie Yamamoto,[2,3] Naohiro Aoyama,[3] Hisao Hamaguchi,[3] Shingo Sugahara,[3] Shinobu Takeda,[3] Varodom Charoensawan,[4,5,6] Atsushi Tanaka,[7] Shimon Sakaguchi,[7] and Shuh Narumiya[1,2,8,11,*]

[1]Department of Drug Discovery Medicine, Kyoto University Graduate School of Medicine, Kyoto 606-8507, Japan
[2]Alliance Laboratory for Advanced Medical Research, Kyoto University Graduate School of Medicine, Kyoto 606-8507, Japan
[3]Drug Discovery Research, Astellas Pharma, Tsukuba, Ibaraki 305-8585, Japan
[4]Department of Biochemistry, Faculty of Science, Mahidol University, Bangkok 10400, Thailand
[5]System Biology of Diseases Research Unit, Faculty of Science, Mahidol University, Bangkok 10400, Thailand
[6]Integrative Computational BioScience (ICBS) Center, Mahidol University, Nakhon Pathom 73170, Thailand
[7]Department of Experimental Immunology, WPI Immunology Frontier Research Center, Osaka University, Osaka 565-0871, Japan
[8]AMED-FORCE, Japan Agency for Medical Research and Development, Chiyoda, Tokyo 100-0004, Japan
[9]These authors contributed equally
[10]Present address: Office of Research, Academic Affairs and Innovation, Faculty of Medicine Ramathibodi Hospital, Mahidol University, Bangkok 10400, Thailand
[11]Lead contact
*Correspondence: d.thumkeo@mfour.med.kyoto-u.ac.jp (D.T.), snaru@mfour.med.kyoto-u.ac.jp (S.N.)
https://doi.org/10.1016/j.celrep.2022.110914

SUMMARY

Active inflammation generally promotes immune activation. However, in the tumor microenvironment (TME), active inflammation occurs in parallel with immunosuppression, and both contribute to tumor growth. Why inflammation does not lead to immune activation in TME remains unclear. In this study, using the immune checkpoint inhibitor-insensitive mouse cancer model and single-cell RNA sequencing, we show that PGE_2-EP2/EP4 signaling simultaneously promotes active inflammation by inducing expression of the NF-κB genes in myeloid cells and elicits immunosuppression by driving the mregDC (mature DC enriched in immunoregulatory molecules)-Treg (regulatory T cell) axis for Treg recruitment and activation in the tumor. Importantly, the EP2/EP4 expression level is strongly correlated with the gene signatures of both active inflammation and the mregDC-Treg axis and has significant prognosis value in various human cancers. Thus, PGE_2-EP2/EP4 signaling functions as the key regulatory node linking active inflammation and immunosuppression in TME, which can be targeted by EP2 and EP4 antagonists for cancer therapeutics.

INTRODUCTION

In the tumor microenvironment (TME), active inflammation often occurs in parallel with immunosuppression (Wang and DuBois, 2015; Palucka and Coussens, 2016; Chen and Mellman, 2017; Greten and Grivennikov, 2019). The former is believed to promote tumor growth and the latter to facilitate the evasion of tumor cells from immune surveillance by acquired immunity (Shalapour and Karin, 2019). However, given that active inflammation in general induces acquired immunity through the activation of dendritic cells (DCs) (Wculek et al., 2020), how immunosuppression is elicited in actively inflamed TME remains an enigma. Interestingly, DCs are often subverted to the immunosuppressive phenotype in TME (Giovanelli et al., 2019).

The immune cells infiltrating the tumor, stromal cells activated in TME, and tumor cells themselves produce and secrete various mediators of diverse functions, which are supposed to trigger inflammation and elicit immunosuppression. One of these factors is prostaglandins (PGs) (Wang and Dubois, 2010; Johnson et al., 2020). It has long been known that the use of non-steroidal anti-inflammatory drugs (NSAIDs), including aspirin, that suppress PG biosynthesis by inhibiting cyclooxygenase (COX) confers prophylactic and therapeutic benefits in cancer patients (Greten and Grivennikov, 2019). Among the PGs, PGE_2 is the most abundant PG produced at tumor sites (Rigas et al., 1993) and exerts its functions through 4 cognate receptors, EP1–EP4 (Sugimoto and Narumiya, 2007). Among many studies on the possible roles of PGE_2 in cancer, some indicate how PGE_2 may suppress cytotoxic T cell (CTL) responses in TME. These include the suppression of antigen presentation by DCs through EP2 (Yang et al., 2003) and the modulation of natural killer (NK)-mediated recruitment of

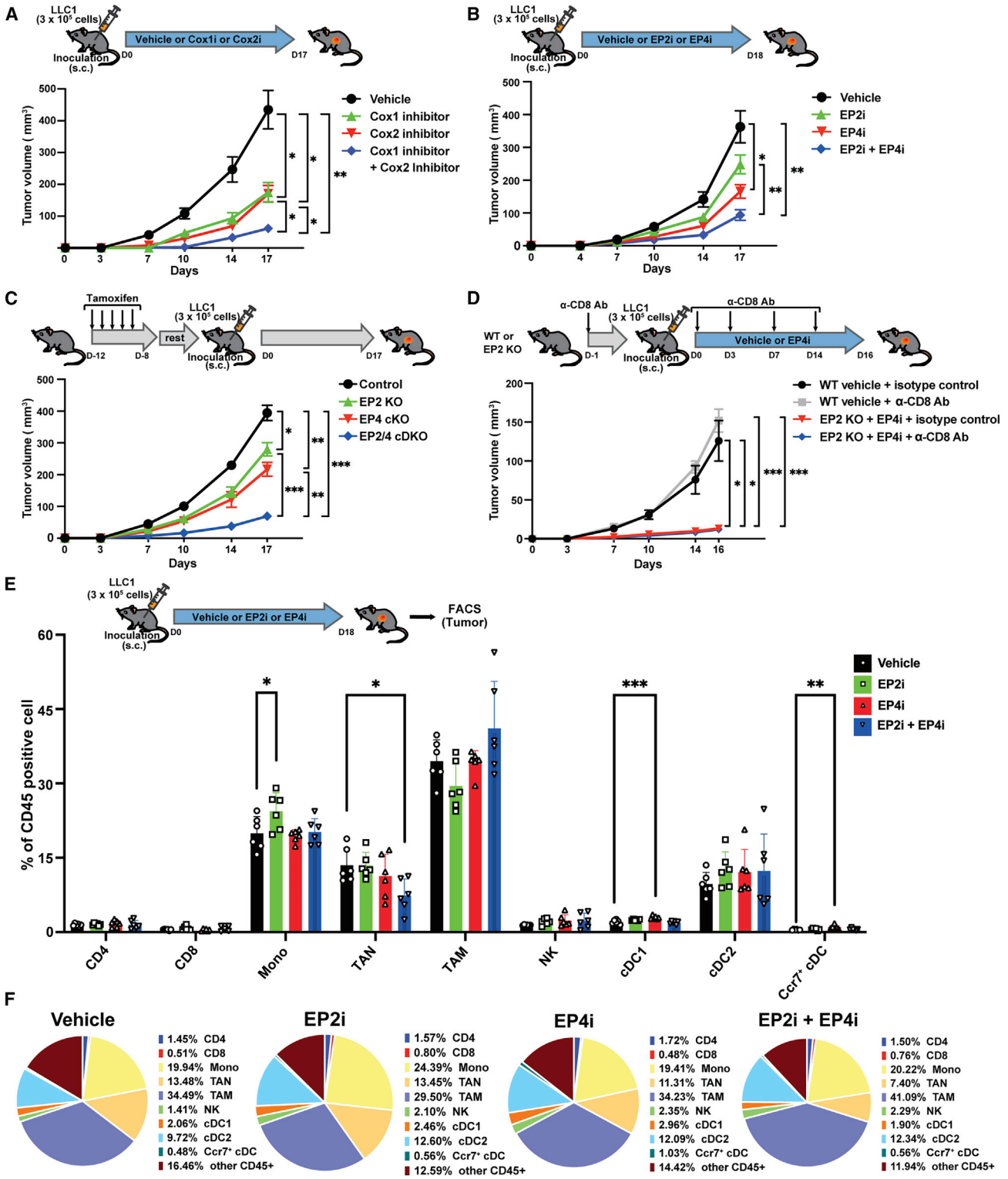

Figure 1. Suppression of LLC1 tumor growth by the inhibition of EP2 and EP4 through the modulation of host immune cells

(A) LLC1 tumor growth in mice treated with vehicle, a Cox1 inhibitor (SC-560, dosed at 30 mg/kg/day, per os [p.o.]), a Cox2 inhibitor (celecoxib, dosed at 30 mg/kg/day, p.o.), or both Cox1 inhibitor and Cox2 inhibitor in combination (n = 8 per each group).

(B) LLC1 tumor growth in mice treated with vehicle, an EP2 antagonist (AS3385282-00, EP2i, dosed at 100 mg/kg/day, p.o.), an EP4 antagonist (ASP7657, EP4i, dosed at 10 mg/kg/day, p.o.), or both EP2 and EP4 antagonists (EP2/4i, dosed at 100 mg/kg/day and 10 mg/kg/day, p.o.) (n = 10 per each group).

(legend continued on next page)

conventional type 1 DC (cDC1) cells through EP2 and EP4 (Zelenay et al., 2015; Bottcher et al., 2018). A more recent report suggests that PGE_2-EP2/4 signaling suppresses interferon-γ (IFN-γ) production of NK cells and subsequent T cell inflammation in immune checkpoint inhibitor (ICI)-sensitive mouse cancer models (Bonavita et al., 2020). In addition, some studies also suggest that PGE_2 reprograms the differentiation of myeloid cells such as tumor-associated macrophages (TAMs) into anti-inflammatory M2 phenotypes rather than activates them for inflammation (Sinha et al., 2007; Albu et al., 2017; Lu et al., 2021). While these studies have provided insights into the potential actions of PGE_2 in TME, they have neither revealed the landscape that PGE_2 shapes in TME nor addressed the question of why cancer-promoting active inflammation does not lead to immune activation, a process in which PGE_2 may play a key role.

To address the above questions, we have investigated the role that PGE_2 plays in TME of the mouse LLC1 (Lewis lung carcinoma 1) syngeneic tumor model, which exhibits active inflammation but is insensitive to ICIs. We have used single-cell RNA sequencing (scRNA-seq) technology combined with pharmacological intervention using EP2- and EP4-specific antagonists, which allows us to identify the immune landscape, phenotypic changes, and cell-cell communications dependent on these EP receptors in TME in an unbiased way. We have then translated our findings in animal models to humans by re-analyzing publicly available human lung cancer scRNA-seq data (Maier et al., 2020) and The Cancer Genome Atlas (TCGA) database of clinical cancers. Our findings demonstrate that PGE_2-EP2/4 signaling promotes inflammation by upregulating the expression of NF-κB components and their targets, proinflammatory and angiogenesis genes, in a wide range of myeloid cells, and simultaneously induces immunosuppression by stimulating the recently identified mregDCs (mature DCs enriched in immunoregulatory molecules) (Maier et al., 2020) and enhancing the production of Ccl22 and Ccl17 to facilitate regulatory T cell (Treg) infiltration and driving TME-specific Treg activation. Furthermore, we show that these PGE_2-mobilized elements are conserved in various human cancers and have significant prognosis value. Our findings thus demonstrate that PGE_2-EP2/EP4 signaling functions as the node linking active inflammation and immunosuppression in TME and may have a significant impact on ongoing clinical trials targeting EP2 and EP4 for cancer patients.

RESULTS

Inhibition of EP2/EP4 suppresses LLC1 tumor growth through modulation of host immune cells

In this study, we used the LLC1 syngeneic tumor model, which we found insensitive to anti-programmed cell death protein 1 (PD-1)-antibody even in the late adaptive phase seen in various mouse tumors (Zelenay et al., 2015) and thus immunosuppressive in the entire course of tumor growth (Figure S1A). We chose the ICI-insensitive tumor to explore PGE_2 mechanisms in TME beyond the previously identified mechanisms in ICI-sensitive models (Zelenay et al., 2015; Bottcher et al., 2018; Bonavita et al., 2020; Lu et al., 2021). The growth of this tumor in mice was suppressed approximately 60% by the administration of either a Cox1 inhibitor, SC-560, or a Cox2 inhibitor, celecoxib, and more strongly by the combination (Figure 1A). These results suggest that both Cox2 and Cox1 are involved in PG production in this tumor and they may act on different pathways to elicit synergy for tumor growth. To validate this finding and explore which PG and PG receptors are involved, we examined the expression of genes of PG-synthesizing enzymes and receptors in this tumor by quantitative RT-PCR analysis (qRT-PCR). LLC1 tumor was resected on day 18 after transplantation and dissociated cells were fluorescence-activated cell sorting (FACS) sorted into $CD45^-$ and $CD45^+$ cells. The expression of *Ptgs1* encoding Cox1 and *Ptgs2* encoding Cox2 was detected in not only $CD45^-$ cells, including tumor cells, but also $CD45^+$ immune cells infiltrating the tumor (Figure S1B). In addition, both $CD45^+$ and $CD45^-$ cell populations expressed PGE-synthesizing enzymes (*Ptges1*) encoding mPGES-1 and *Ptges2* encoding mPGES-2. These findings suggest that PGE_2 is produced by both tumor cells and non-tumor cells in this tumor (Figure S1B), which is consistent with a report that LLC1 cells produce high levels of PGE_2 *in vitro* (Liu et al., 2012a, 2012b). However, among four EP subtypes, *Ptger2* encoding EP2 and *Ptger4* encoding EP4 were highly and dominantly expressed in $CD45^+$ immune cells (Figure S1B). *Ptger3* encoding EP3 was expressed in both $CD45^+$ and $CD45^-$ cell populations at intermediate levels and *Ptger1* encoding EP1 only at low levels in both $CD45^+$ and $CD45^-$ cell populations (Figure S1B).

Based on these findings, we examined the effects of an EP2 antagonist, AS3385282-00 (EP2i); an EP4 antagonist, ASP7657 (EP4i) (Mizukami et al., 2018); and the two antagonists in combination (EP2/4i) on the LLC1 tumor growth. AS3385282-00 is a small-molecule compound (Figure S1C), with half-maximal

(C) LLC1 tumor growth in control wild-type (WT) mice (n = 10), EP2 KO mice (n = 7), EP4 cKO mice (n = 4), or EP2/EP4 cDKO mice (n = 4). Conditional knockout of EP4 in UBC-CreERT2 x EP4 floxed mice and conditional double knockout of EP2 and EP4 in UBC-CreERT2 x EP2/EP4 double floxed mice were induced by daily intraperitoneal (i.p.) injection of tamoxifen for 5 days. After the last injection, mice were left resting for 1 week. LLC1 tumor cells were then transplanted to the right flank of the mice.

(D) LLC1 tumor growth in WT mice treated with vehicle and isotype control immunoglobulin G (IgG) (dosed at 100–200 μg/mouse, i.p.) or vehicle and anti-CD8 antibody (dosed at 100–200 μg/mouse, i.p.), and EP2 KO mice treated with EP4i (dosed at 10 mg/kg/day, p.o.) and isotype control IgG dosed as above or EP4i dosed as above and anti-CD8 antibody dosed as above (n = 9 per each group).

(E) Composition of LLC1 tumor-infiltrating $CD45^+$ immune cells analyzed by FACS on day 18 after tumor cell transplantation in mice treated with vehicle (control), EP2i (dosed at 100 mg/kg/day, p.o.), EP4i (dosed at 1 mg/kg/day, p.o.), and EP2i dosed as above and EP4i dosed as above in combination. Data are shown as means ± SDs (n = 6 per each group) and the statistical analyses were conducted using 1-way ANOVA with Dunnett's test compared to the control. $^*p < 0.05$; $^{**}p < 0.01$; $^{***}p < 0.001$.

(F) Frequencies of each immune cell per $CD45^+$ cells in (E) are shown. n = 6 per each group.

In (A)–(D), data are shown as means ± SEMs, and statistical analyses were conducted using 2-way ANOVA with Tukey's correction for multiple testing. Statistical significances at the endpoint are shown. $^*p < 0.05$; $^{**}p < 0.01$; $^{***}p < 0.001$.

inhibitory concentration (IC_{50}) values on cyclic AMP (cAMP) responses to human EP2, EP4, and rat EP2 of 0.79 nM, 9.1 μM, and 1.3 nM, respectively (Figure S1D), and showing full antagonism to EP2 agonist-induced blood pressure reduction in mice at 100 mg/kg (Figure S1E). While treatment with EP2i or EP4i or EP2/4i did not affect the LLC1 cell viability *in vitro* (Figure S1F), *in vivo* treatment with EP2i or EP4i suppressed tumor growth, and treatment with EP2/4i further suppressed the growth (Figures 1B and S1G). Notably, compared to the tumor dissected from the control mice, tumors dissected from mice treated with EP2/4i were not only smaller but also paler (Figure S1H). The EP2 and EP4 antagonists exerted this antitumor effect by acting on the host cells and not the transplanted LLC1 tumor cells, because EP2 knockout (EP2 KO), EP4 conditional knockout and EP2/EP4 conditional double knockout mice mimicked the tumor-suppressive effects of each antagonist (Figures 1C and S1I). These findings suggest that PGE_2 promotes tumor growth by acting on the EP2 and EP4 expressed in the tumor-infiltrating $CD45^+$ immune cells, and that the EP2 and EP4 antagonists exert their antitumor effects by blocking these actions. Interestingly, the $CD8^+$ T cell depletion did not significantly affect the tumor suppression by the blockade of EP2/4 (in this case, EP4i administered to EP2 KO mice) (Figures 1D and S1J), suggesting that the host immune cells other than $CD8^+$ T cells make major contributions to the EP2/4 inhibition-induced suppression of LLC1 tumor growth under the current treatment conditions.

We then conducted FACS analysis of immune cells infiltrating the tumors grown in mice treated with vehicle, EP2i, EP4i, or EP2/4i, and examined relative proportions of $CD4^+$ and $CD8^+$ T cells, NK cells, tumor-infiltrating monocytic cells (Mono; $CD45^+CD11b^+F4/80^-Ly6C^{hi}Ly6G^-$), tumor-associated neutrophils (TAN; $CD45^+CD11b^+F4/80^-Ly6C^{lo}Ly6G^+$), tumor-associated macrophages (TAM; $CD45^+CD11b^+F4/80^+Ly6C^-Ly6G^-$), cDC1 ($CD45^+lin^-I\text{-}A/I\text{-}E^+CD11c^+CD11b^-Ccr7^-$), cDC2 ($CD45^+lin^-I\text{-}A/I\text{-}E^+CD11c^+CD11b^+Ccr7^-$), $Ccr7^+$ cDC ($CD45^+lin^-I\text{-}A/I\text{-}E^+CD11c^+Ccr7^+$), and other $CD45^+$ immune cells. This analysis showed (1) no significant difference in the percentage of tumor-infiltrating $CD45^+$ immune cells to live cells among the 4 groups of mice (Figure S1K) and (2) no large change in the proportions of various $CD45^+$ cell populations in the EP2/4i-treated mice from the control mice, except a significant decrease in TAN in EP2/4i-treated mice (Figures 1E and 1F). The other changes that we observed compared to control mice include a significant increase in Mono in EP2i-treated mice and a significant increase in cDC1 and $Ccr7^+$ cDC in EP4i-treated mice (Figures 1E and 1F). Therefore, the blockade of EP2/4 in combination slightly reduced the number of TAN, but did not drastically change the composition of other immune cells infiltrating the LLC1 tumor.

scRNA-seq analysis unravels immune landscape in LLC1 tumor and identifies cell populations expressing *Ptger2* and *Ptger4*

We next examined the therapeutic effect of EP2 and EP4 antagonists on the LLC1 tumor of ~17–34 mm^3 size, and found that EP2/4i also significantly suppressed tumor growth in this experimental setting (Figure 2A). We then used scRNA-seq on the tumors to dissect the actions of PGE_2-EP2/4 signaling on heterogeneous tumor-infiltrating immune cell populations upon the treatment with the antagonists (Figure 2B). We prepared single-cell suspensions of LLC1 tumors treated with vehicle (n = 2), EP2i (n = 1), EP4i (n = 1), and EP2/4i (n = 2) for 6 days (Figures S2A–S2C). $CD45^+$ tumor-infiltrating immune cells were then sort purified and subsequently loaded onto the 10x Chromium system, and 10,000 cells per mouse were randomly captured. Single-cell library preparation and sequencing were performed according to the manufacturer's recommendations (see Method details). After pre-processing and quality control, there were a total of 9,673, 6,143, 4,397, and 11,758 cells from the tumors treated with vehicle, EP2i, EP4i, and EP2/4i, respectively, for further downstream analysis (Figure 2C). Applying unsupervised clustering to the integrated scRNA-seq data (31,971 cells), we were able to identify 15 clusters with unique expression patterns (Figures 2D and S2D). We determined the cell-type identities of these clusters by their gene expression signatures based on publicly available database ImmGen (https://www.immgen.org) and a recent publication (Maier et al., 2020). The genes representative of each cell type/subtype/state are shown in Figures 2E and S2D. Specifically, the LLC1 tumor-infiltrating DCs consist of 4 subtypes/states: "cDC1s" expressing *Xcr1*, *Cd103*, and *Blta*; "cDC2s" expressing *Cd11c* and major histocompatibility complex (MHC) class II molecules; "cDCs of mregDC state (mregDCs)" expressing *Ccr7*, *Il12β*, and *Ccl22*; and "pDCs" expressing *Siglec-h*, *Ccr9*, and *Cd300c*. For the lymphocytes, "NK cells" expressing *Nkg7*, *Gzma*, and *Gzmb*; "T cells" expressing *Cd3d* and *Il2rβ*; and "B cells" expressing *Ighd* and *Cd79b* were identified. For the myeloid cells, TANs consist of two subtypes: "TAN s1" expressing *Retnlg*, *Arg2*, and *Cxcr2* and "TAN s2" expressing *Cxcl3*, *Vcan*, and *Cxcl1*. The tumor-infiltrating Monos consist of 4 subtypes: "Mono s1" expressing *Irf7*, *Ifi203*, and *Mx1*; "Mono s2" expressing *Spp1* and *Tgfβ1*; "Mono s3" expressing *Axl* and MHC class II molecules; and "Mono s4" expressing *Ccl9*, *Arg1*, and *Vegfa*. TAMs consist of two subtypes: "TAM" expressing *Adgre1* (encoding F4/80), *C1qa*, and *Ccl7*, and "proliferating TAM (prolif TAM)" expressing *Mki67* and *Hist1h3c*. To identify the potential targets of EP2 and EP4 antagonists, we examined the abundance of *Ptger2* and *Ptger4* transcripts (Figure 2F). Both *Ptger2* and *Ptger4* transcripts were detected in a fraction of T cell, TAN s1 and s2, Mono s1–s4, TAM, and proliferating TAM. Notably, EP4 was expressed at a high level in most *Ccr7* expressing mregDCs and at an intermediate level in a fraction of cDC1s, cDC2s, and pDCs.

PGE_2-EP2/4 signaling in myeloid cells amplifies active inflammation in LLC1 TME through NF-κB signaling

Given the expression of both EP2 and EP4 in the TAN, Mono, and TAM populations, we performed differential expression gene (DEG) analysis in these myeloid cell populations between the control and EP2/4i-treated samples. We found numerous DEGs in each population (Figure S2E; Table S1), suggesting that EP2/4 inhibition induced drastic changes in gene expression in these myeloid cells. Notably, proinflammatory genes such as *Ptgs2* and *Il1b* and inflammation-associated angiogenesis genes such as *Vegfa* and *Hif1a* were significantly downregulated upon the EP2/4i treatment (Figures S2F–S2L). Since *Ptgs2*, *Il1b*, and *Hif1a* are NF-κB target genes (Pahl, 1999), we further generated

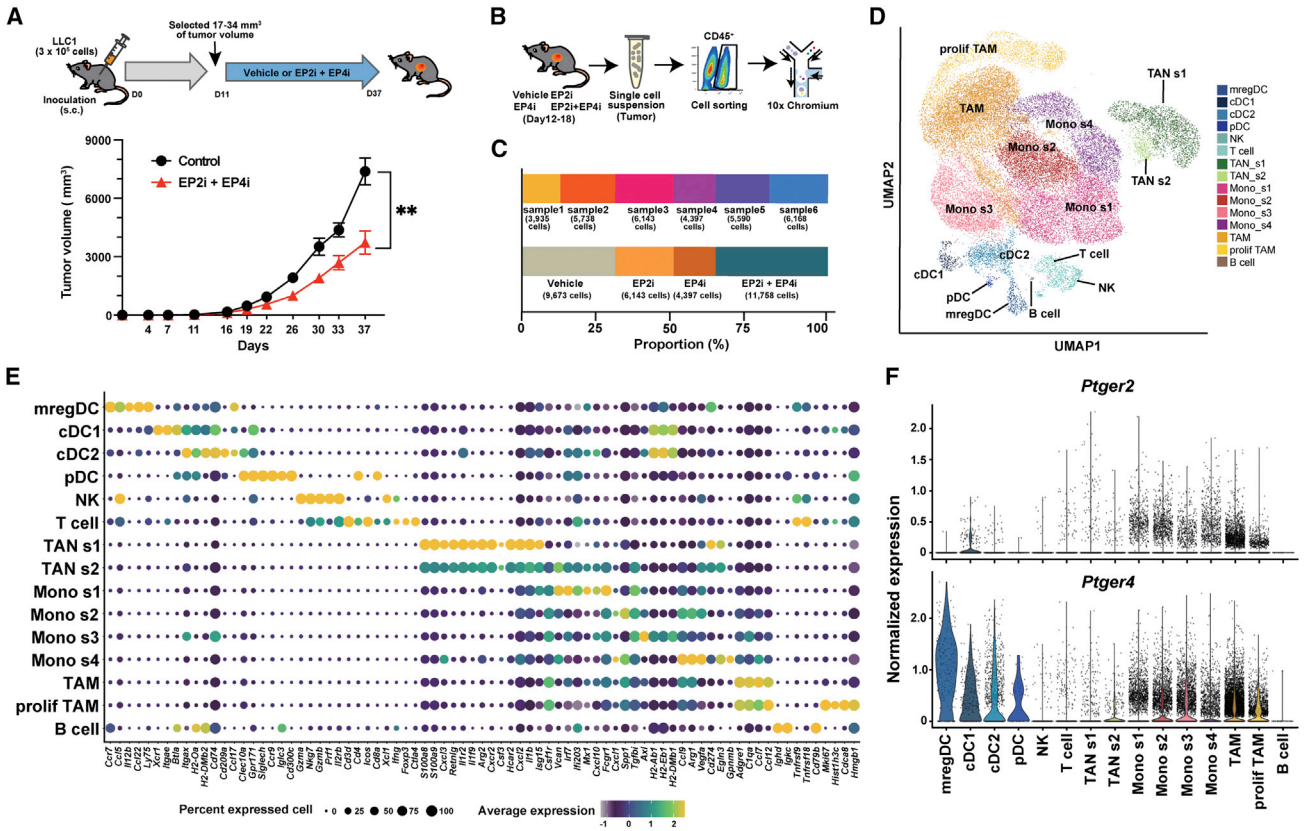

Figure 2. scRNA-seq analysis of tumor-infiltrating CD45$^+$ immune cells in the LLC1 tumor and their *Ptger2* and *Ptger4* expression

(A) Growth suppression of LLC1 tumor by therapeutic application of the EP2 and EP4 antagonists. Mice were treated with the EP2i and EP4i (dosed at 100 mg/kg/day and 1 mg/kg/day, respectively, both p.o.) from day 11 after LLC1 transplantation and growth was monitored to day 37. n = 6 for each group. Data are shown as means ± SEMs, and the statistical analysis was conducted at the endpoint using an unpaired 2-tailed t test. **$p < 0.01$.

(B) Schematic overview of the single-cell RNA sequencing experiment.

(C) Distribution of the cell number from each sample after filtering (top) and each condition after integration of samples from the same treatment (bottom).

(D) UMAP plot of tumor-infiltrating CD45$^+$ immune cell clusters.

(E) Dot plot showing the expression of discriminatory marker genes for each cell population in (D).

(F) Violin plots showing the gene expression distribution of *Ptger2* and *Ptger4* in each identified cell population.

a dot plot for the expression of genes targeted by NF-κB (Yang et al., 2016) and/or genes involved in inflammation-associated angiogenesis (Vasse et al., 1999). Intriguingly, treatment with EP2/4i largely suppressed their expression in all myeloid populations, with the strongest suppression in the TAN population (Figure 3A). We then validated DEG results by qRT-PCR analysis of sort-purified tumor-infiltrating TAN and confirmed that the expression of *Hif1a*, *Vegfa*, *Il1b*, and *Ptgs2* was significantly downregulated upon the blockade of EP2 and EP4 (Figure 3B). In addition, the expression of these genes in tumor-infiltrating monocytic cells and TAM was also downregulated upon the blockade of EP2 and EP4 (Figures S2M and S2N). Furthermore, the expression of genes encoding several components of the NF-κB complex, including *Rela*, *Nfkb1*, and *Nfkbiz* was also downregulated in all tumor-infiltrating myeloid cells (Figure 3C). We then conducted gene set enrichment analysis (GSEA) for Gene Ontology (GO) terms (Subramanian et al., 2005) on the integrated myeloid cells (TAN s1 and s2, Mono s1–s4, and TAM). While EP2/4i treatment significantly downregulated a number of gene sets in the myeloid cells (Figure S2O; Table S2), top-ranked gene sets included those related to angiogenesis (Figure 3D). This result suggests that inflammatory myeloid cells mediate angiogenesis in an EP2/4-dependent manner in LLC1 tumors. We therefore performed CD31 immunohistochemistry in LLC1 tumors to evaluate the impact of the EP2/4i treatment on tumor blood vessel formation (Figure 3E). Quantitative results showed that the vascular density as measured by the percentage of the CD31-stained area was significantly reduced upon EP2/4i treatment (Figure 3F). These results together suggest that PGE_2-EP2/EP4 signaling enhances NF-κB-mediated active inflammation/angiogenesis responses in tumor-infiltrating myeloid cells, and EP2/EP4 antagonists can suppress this process.

PGE_2-EP2/4 signaling mediates immunosuppression in inflammatory LLC1 TME through the production of Ccl22 and Ccl17 by mregDCs that promote Treg infiltration

Given the high expression of *Ptger4* in the *Ccr7*-expressing mregDCs (Figure 2F), we conducted DEG analysis of this state

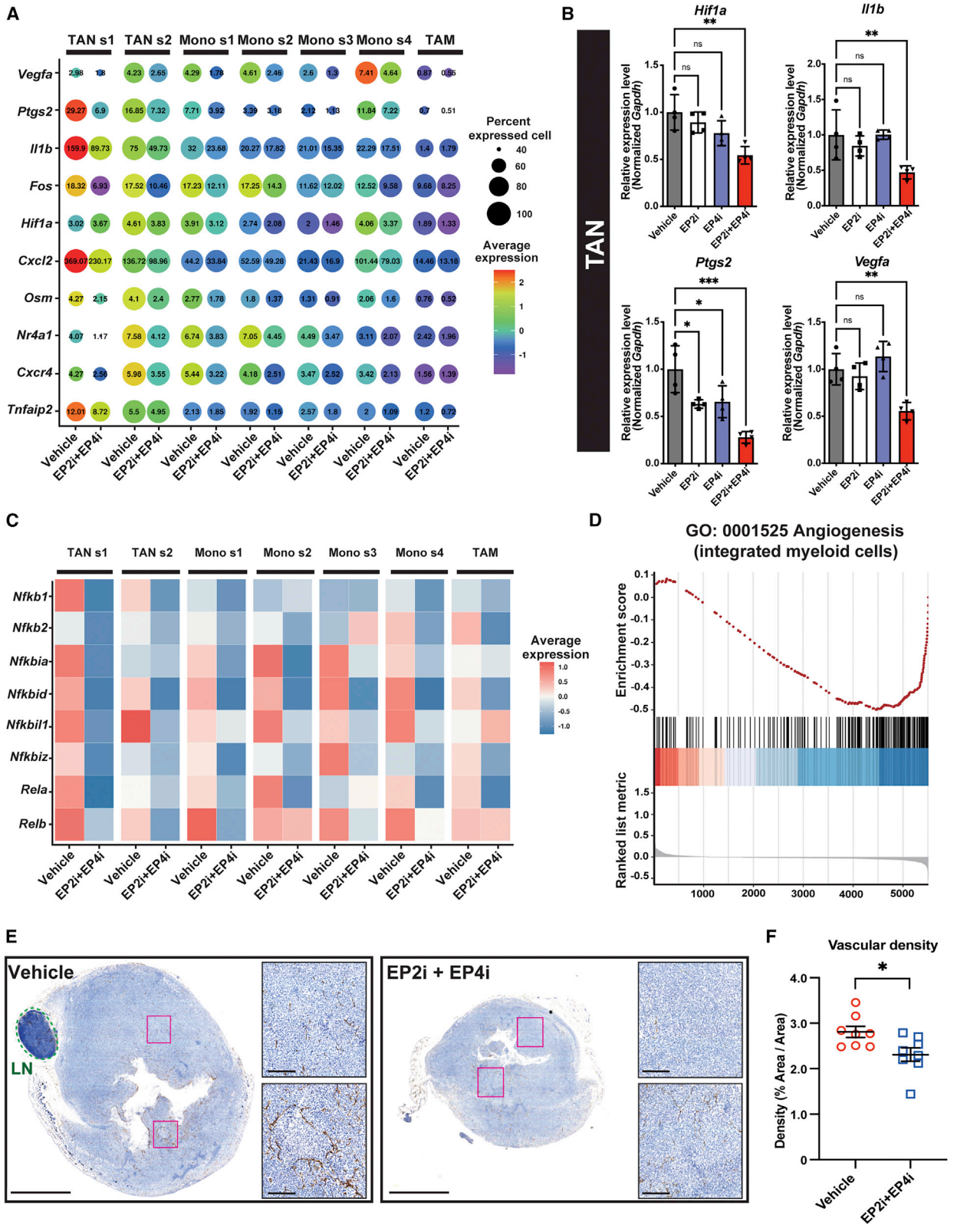

(legend on next page)

of DCs and found a number of genes suppressed by EP2/4i as compared to the controls (Figure S3A; Table S3). Notably, the chemokine *Ccl22* was strongly and significantly downregulated in mregDCs of EP2/4i-treated mice (Figures 4A and S3A). Given that Ccl22 and another chemokine, Ccl17, attract Treg cells (Yoshie and Matsushima, 2015), we sort purified Ccr7$^+$ cDCs together with cDC2, TAM, and CD45$^-$ cells from the tumors from control and EP2/4i-treated mice, cultured them, and then measured the amounts of Ccl22 and Ccl17 in their culture supernatants. Among the cell populations tested, Ccr7$^+$ cDCs produced by far the highest levels of Ccl22 and Ccl17, followed by cDC2, and the production of both Ccl22 and Ccl17 in the Ccr7$^+$ cDCs was significantly reduced by the EP2/4i treatment (Figure 4B). We then depleted Ccl22 and Ccl17 in LLC1-bearing mice by administering neutralizing antibodies to Ccl22 and Ccl17 and determined the tumor size and the number of tumor-infiltrating Tregs with a group of EP2/4i-treated mice for comparison. Neutralization of Ccl22 and Ccl17 significantly reduced tumor growth (Figure 4C) concomitant with a significant reduction in the number of tumor-infiltrating Tregs (Figure 4D). Notably, the EP2/4i treatment also reduced the number of tumor-infiltrating Tregs with reduced tumor size (Figures 4C and 4D). These results suggest that the PGE_2-EP2/4 signaling increases Ccl22 and Ccl17 production by Ccr7$^+$ cDCs, thereby recruiting Tregs to LLC1 tumors for tumor growth.

PGE_2-EP2/4 signaling promotes tumor Treg stability and enhances its suppression activity

Based on the scRNA-seq data, we next subclustered the tumor-infiltrating T cells to non-Treg CD4, CD8, Treg, and proliferating T subsets (Figures S3B and S3C) and examined the DEGs of tumor-infiltrating Tregs between control and EP2/4i-treated tumors (Figure S3D). Intriguingly, several Treg signature genes, including *Foxp3*, *Stat5b*, *Il2ra*, and *Ctla4* (Sakaguchi et al., 2020) were downregulated upon EP2/4i treatment (Figure 4E). Moreover, genes reported to be specifically upregulated in tumor-infiltrating Tregs (Freeman et al., 2020), such as *Tnfrsf4* (encoding Ox40), *Tnfrsf9* (encoding 4-1bb), and *Tnfrsf18* (encoding Gitr) were also strongly downregulated by the EP2/4i treatment (Figure 4E). Consistently, FACS analysis revealed that EP2/4i treatment of LLC1 tumor-bearing mice significantly reduced the percentage of 4-1bb$^+$ Treg in TME (Figure 4F). These results therefore suggest that the PGE_2-EP2/4 signaling not only increases the number of Treg but also activates tumor-infiltrating Treg in the LLC1 tumor model.

To verify the above findings experimentally, we examined the effects of PGE_2 on the stability of *in vitro*-induced (i) Tregs using a published protocol (Mikami et al., 2020) (Figure 4G). PGE_2 promoted iTreg stability *in vitro* as measured as the retention of Foxp3 expression and EP2/4i treatment blocked this PGE_2-mediated stabilization (Figure 4H). In contrast, PGE_2 suppressed iTreg differentiation from naïve CD4$^+$ T cells in an EP2/4-dependent manner (Figures S3E and S3F). Therefore, PGE_2 exerted the opposite effects on iTregs, depending on their stages. Moreover, PGE_2 significantly increased the surface expression of 4-1bb in iTregs in an EP2/4-dependent manner *in vitro* (Figure 4I). These findings suggest that in addition to its action on mregDCs, PGE_2-EP2/4 signaling possibly stabilizes and activates Tregs directly in tumors, and inhibition of EP2/EP4 suppresses these processes and impairs Treg functions.

EP2/4i treatment shares in part activation of CD4$^+$ and CD8$^+$ T cells and IFN responses with Treg depletion in LLC1 tumors

The above findings then led us to investigate how much Tregs contribute to the LLC1 tumor growth and to what extent EP2/4 signaling plays a role in this process. To this end, we transplanted LLC1 tumors in Foxp3-DTR/EGFP mice (Kim et al., 2007) and depleted Tregs using diphtheria toxin (DT) (Figure S3G). DT-mediated Treg depletion strongly suppressed LLC1 tumor growth to a level comparable to that of EP2/4i (Figure S3H). Moreover, EP2/4i treatment induced an additional suppression of tumor growth to Treg depletion (Figure S3H). FACS analysis revealed that the numbers of CD4$^+$ and CD8$^+$ T cells in tumors increased in association with Treg depletion for 14 days (Figure S3I, left), and these cells exhibited higher Gzmb expression than those in vehicle-treated mice (Figure S3I, right). The numbers of CD4$^+$ and CD8$^+$ T cells and their Gzmb

Figure 3. Inhibition of EP2 and EP4 suppresses gene expression of NF-κB targets and components in a wide range of myeloid cells and dampens active inflammation in LLC1 tumor

(A) Dot plot based on scRNA-seq analysis showing scale average expression level of representative NF-κB target genes by myeloid cell populations (TAN, Mono, and TAM) in LLC1 tumor of control WT mice treated with vehicle or treated with EP2i (dosed at 100 mg/kg/day) and EP4i (dosed at 1 mg/kg/day) in combination (EP2i + EP4i) (n = 2 per group) for 6 days.

(B) qRT-PCR analysis for *Hif1a*, *Il1b*, *Ptgs2*, and *Vegfa* expression in TANs (CD45$^+$CD11b$^+$F4/80$^-$Ly6C^{lo}Ly6G$^+$) from LLC1 tumor of WT mice treated with vehicle, EP2i (dosed at 100 mg/kg/day), EP4i (dosed at 1 mg/kg/day), or EP2i and EP4i dosed as above in combination for 17 days (n = 4 per group). Normalized fold changes to *Gapdh* are shown. Data are shown as means ± SDs, and statistical analyses were conducted using 1-way ANOVA with Dunnett's test compared to the control. ns, not significant; *p < 0.05; **p < 0.01; ***p < 0.001.

(C) Heatmap based on scRNA-seq analysis of NF-κB component genes expressed by myeloid cell populations in LLC1 tumors of control WT mice treated with vehicle or EP2i and EP4i in combination administered as in (A) (n = 2 per group). Average expression represented scale expression using *Z* score within each cell type.

(D) GSEA of the DEGs between myeloid cells from mice treated with EP2/4i and control mice based on scRNA-seq analysis. Shown is a representative of the negatively regulated "hallmark" signatures that are involved in the angiogenesis process.

(E) Representative images of immunohistochemistry staining of CD31 (brown) in LLC1 tumor tissue of WT mice treated with vehicle or EP2i (dosed at 100 mg/kg/day, p.o.) and EP4i (dosed at 10 mg/kg/day, p.o.) in combination (n = 8 mice per group). Scale bars, 2.5 mm (low magnification) and 250 μm (high magnification). LNs (lymph nodes) adjacent to the tumor are encircled by green dashed line.

(F) Quantitative analysis of vascular density measured as percentage of CD31$^+$ area/total area as in (E) (n = 8 mice per group). Data are shown as means ± SEMs, and statistical analysis was conducted using unpaired 2-tailed t test. *p < 0.05.

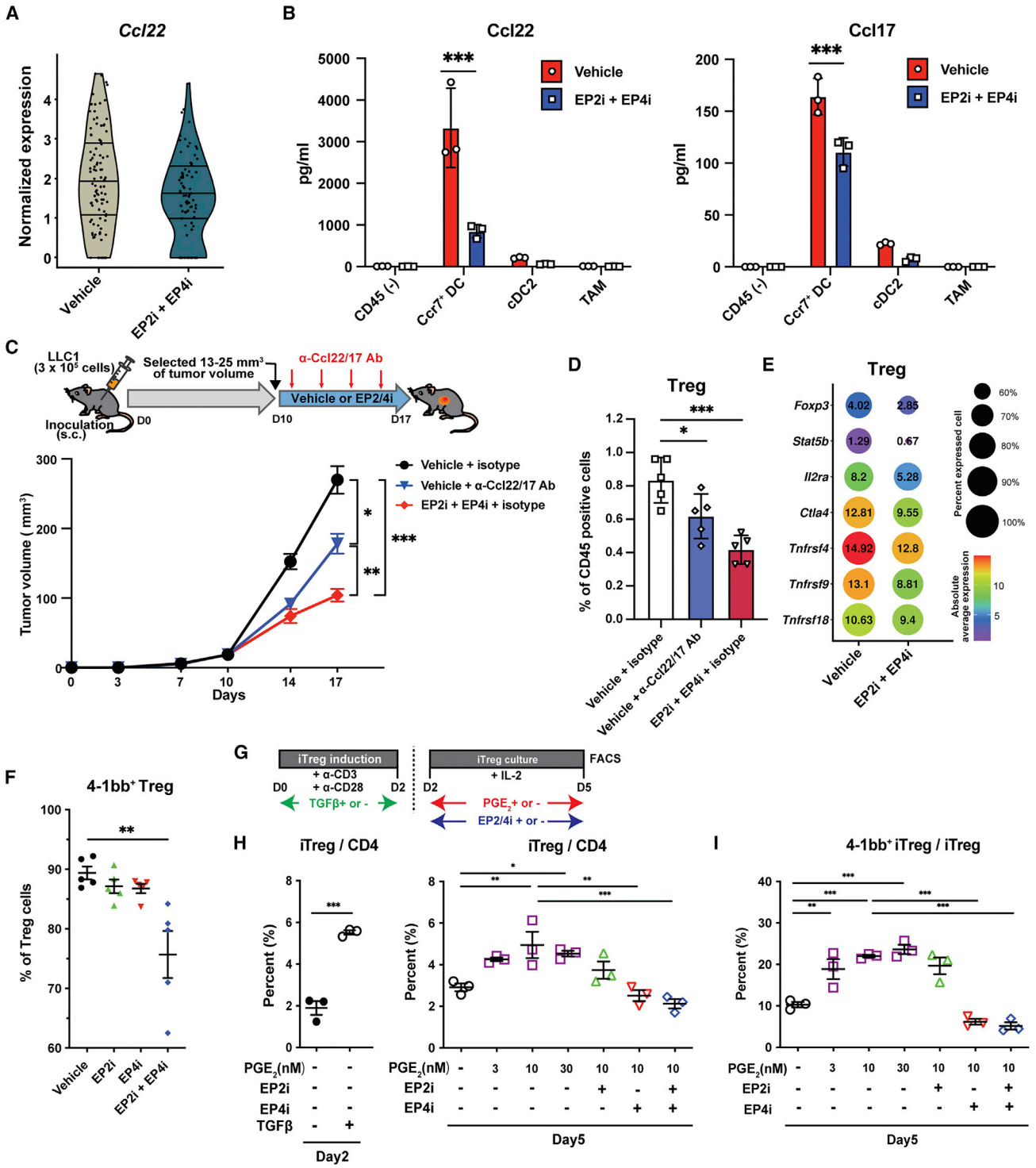

Figure 4. Inhibition of EP2 and EP4 impairs Treg infiltration and activation in LLC1 tumor

(A) Violin plot based on scRNA-seq analysis showing the gene expression distribution of *Ccl22* in mregDC from the vehicle group and the EP2/4i-treated group (n = 2, each group).

(B) Production of Ccl22 (left) or Ccl17(right) by sort-purified Ccr7$^+$ cDC, cDC2, and CD45$^-$ cells and TAM from LLC1 tumor on day 15 of WT mice treated with vehicle or EP2i (dosed at 100 mg/kg/day, p.o.) and EP4i (dosed at 1 mg/kg/day, p.o.) in combination. Sorted cells were cultured in the presence of LPS (1 μg/mL) for 36 h, and the amounts of the chemokines in the supernatants were measured by LEGENDplex (n = 3 per each group). Data are shown as means ± SDs, and statistical analyses were conducted using two-way ANOVA with Bonferroni's test. ***p < 0.001.

(legend continued on next page)

expression also tended to increase in the tumor of EP2/4i-treated mice, although they did not reach statistical significance (Figure S3J). These results are consistent with the role of EP2/4 signaling in Treg recruitment and activation, but suggest that the EP2/4i treatment under the present experimental conditions was not sufficient to fully attenuate the Treg activity in this tumor model.

To obtain the overall landscape induced by Treg depletion in LLC1 tumors, we conducted scRNA-seq analysis of tumors after Treg depletion (Figure S3K, top). We obtained a total of 8,376 cells from the control group (n = 2), and 9,397 cells from the Treg-depleted group (n = 2) for downstream analysis (Figure S3K, bottom). Unsupervised clustering of integrated scRNA-seq data (17,773 cells) identified 15 clusters as shown in the uniform manifold approximation and projection (UMAP) plot (Figure S3L). We examined their gene expression signatures (Figure S3M), and identified 4 DC populations, cDC1, cDC2, mregDC, and pDC; a lymphocyte population containing T cells and NK cells; a TAN population; 4 tumor-infiltrating monocyte populations (Mono 1–4); 2 TAM populations (TAM and proliferating TAM); an endothelial cell population; a fibroblast population; and an epithelial cell population. The percentages of these cell populations in the control and Treg-depleted mice are shown in Figure S3N. Gene expression analysis revealed that, consistent with our qRT-PCR analysis (Figure S1B), *Ptgs1, Ptgs2, Ptges1*, and *Ptges2* were expressed in both immune and non-immune cells, but *Ptger2* and *Ptger4* expression was again almost exclusively expressed in tumor-infiltrating immune cells (Figure S3O). Notably, DEG analysis detected the upregulation of a large number of interferon-stimulated genes (ISGs) stimulated by not only type II but also type I IFNs (Liu et al., 2012a, 2012b) in integrated myeloid cells (TAN, Mono 1–4, and TAM) of Treg-depleted mice (Figure S3P), suggesting that the production of IFNs is another mechanism for tumor suppression by Treg depletion. Intriguingly, EP2/4i treatment also upregulated a series of type I/II ISGs in integrated myeloid cells (Figure S3Q) and in several tumor-infiltrating cell populations, including mregDC, cDC1, NK cells, and T cells (Figure S3R). Therefore, it is likely that the EP2/4i treatment gains therapeutic benefits also from liberating IFN responses, as does Treg depletion.

scRNA-seq analysis at day 1.5 after EP2/4i treatment reveals the rapid change of tumor-infiltrating immune cell transcriptional profiles

To investigate the transcriptional profiles of tumor-infiltrating immune cell change upon EP2/4i treatment at early time points, we additionally conducted scRNA-seq at day 1.5 after EP2/4i treatment (Figure S4A). We obtained a total of 9,638 and 25,074 cells from the control (n = 3) and EP2/4i-treated (n = 3) group, respectively, for analysis (Figure S4B). Unsupervised clustering of integrated scRNA-seq data (34,712 cells) identified 15 clusters as shown in the UMAP plot (Figure S4C) similar to those in the analysis at day 6 in Figure 2D. Based on their gene signatures (Figure S4D), we identified 4 DC populations (cDC1, cDC2, mregDC, and pDC), 1 T cell population, 1 NK cell population, 2 TAN populations, 4 monocytic cell populations, 2 TAM populations, TAM, and proliferating TAM (Figures S4C and S4D).

By analyzing the expression of inflammatory/angiogenesis genes in myeloid populations, we found that they were consistently suppressed at this early time point upon EP2/4i treatment (Figure S4E), as we observed in the 6-day treatment (Figure 3A). Furthermore, the expression of genes encoding components of the NF-κB complex was also downregulated in all tumor-infiltrating myeloid cells (Figure S4F), as in Figure 3C. These results suggest that EP2/4i treatment suppressed active inflammation and angiogenesis from the early time point of the treatment.

We next examined the effect of this 1.5-day EP2/4i treatment on the mregDC-Treg axis. We analyzed the expression of *Ccl22* in the mregDC population and found that it was strongly suppressed (Figure S4G), similar to the 6-day treatment (Figure 4A).

(C) LLC1 tumor growth in WT mice treated with vehicle and isotype control IgG (dosed at 20 μg/mouse, i.p.), vehicle and anti-Ccl22 and anti-Ccl17 neutralization antibody (dosed at 20 μg/mouse, i.p.), or EP2i (dosed at 100 mg/kg/day, p.o.) and EP4i (dosed at 1 mg/kg/day, p.o.) in combination and isotype control IgG (dosed at 20 μg/mouse, i.p.). After transplanted LLC1 tumor reached ~13–25 mm^3, anti-Ccl22 and anti-Ccl17 antibodies were injected i.p. every 2 days, or EP2i and EP4i were orally administered daily (n = 5 per each group). Data are shown as means ± SEMs, and the statistical analysis was conducted using two-way ANOVA with Tukey's correction for multiple testing. Statistical significances at the endpoint are shown. *p < 0.05; **p < 0.01; ***p < 0.001.

(D) Percentage of tumor-infiltrating Tregs in $CD45^+$ cells from the tumor shown in (C) was determined by FACS analysis at day 17 (n = 5 per each group). Data are shown as means ± SEMs, and the statistical analysis was conducted using 1-way ANOVA with Tukey's multiple comparisons test. *p < 0.05; ***p < 0.001.

(E) Dot plot based on scRNA-seq analysis showing absolute average expression level of Treg signature genes (*Foxp3*, *Stat5b*, *Il2ra*, and *Ctla4)* and genes highly expressed in tumor-infiltrating Treg (*Tnfrsf4*, *Tnfrsf9*, and *Tnfrsf18)* of Treg subpopulation of vehicle-treated control group (n = 2) and EP2 and EP4 antagonist-treated group (n = 2).

(F) Percentage of 4-1bb-expressing Tregs in LLC1 tumors of WT mice treated with vehicle, EP2i (dosed at 100 mg/kg/day, p.o.), EP4i (dosed at 1 mg/kg/day, p.o.), or EP2i and EP4i dosed as above in combination for 17 days after tumor transplantation was determined by FACS analysis (n = 5 per each group). Data are shown as means ± SEMs, and the statistical analysis was conducted using 1-way ANOVA with Dunnett's test compared to the control. **p < 0.01.

(G) Schematic representation of the iTreg stability experiment *in vitro*. Magnetic-activated cell sorting (MACS)-purified splenic naive $CD4^+$ T cells were stimulated with anti-CD3 antibodies (10 μg/mL) and anti-CD28 antibodies (1 μg/mL) with or without transforming growth factor-β1 (TGF-β1) (5 ng/mL) for 2 days to induce iTregs. After the induction of iTregs as $Foxp3^+$ cells were confirmed by FACS analysis, the whole cells were washed once and further incubated with PGE_2 (3, 10, or 30 nM) or 10 nM PGE_2 in the presence of EP2i (300 nM) or EP4i (300 nM) or both for an additional 3 days, and subjected to the analysis for $Foxp3^+$ CD4 T cells (iTreg) and $Foxp3^+4\text{-}1bb^+$ CD4 T cells (4-$1bb^+$ iTreg) (n = 3 per group).

(H) Percentage of Foxp3 $^+$ iTreg cells in $CD4^+$ T cells. Data are shown as means ± SEMs (n = 3 per group), and statistical analyses at day 2 were conducted using unpaired 2-tailed t test and at day 5 were conducted using 1-way ANOVA with Tukey's correction for multiple testing. Only the statistical differences for the comparison with the non-treated control group or the comparison with the 10 nM PGE_2-treated group are shown. *p < 0.05; **p < 0.01; ***p < 0.001.

(I) Percentage of 4-1bb-expressing iTregs as determined by FACS analysis. Data are shown as means ± SEMs (n = 3 per group), and the statistical analysis was conducted using 1-way ANOVA with Tukey's correction for multiple testing. Only the statistical differences for the comparison with the non-treated control group or the comparison with the 10 nM PGE_2-treated group are shown. **p < 0.01; ***p < 0.001.

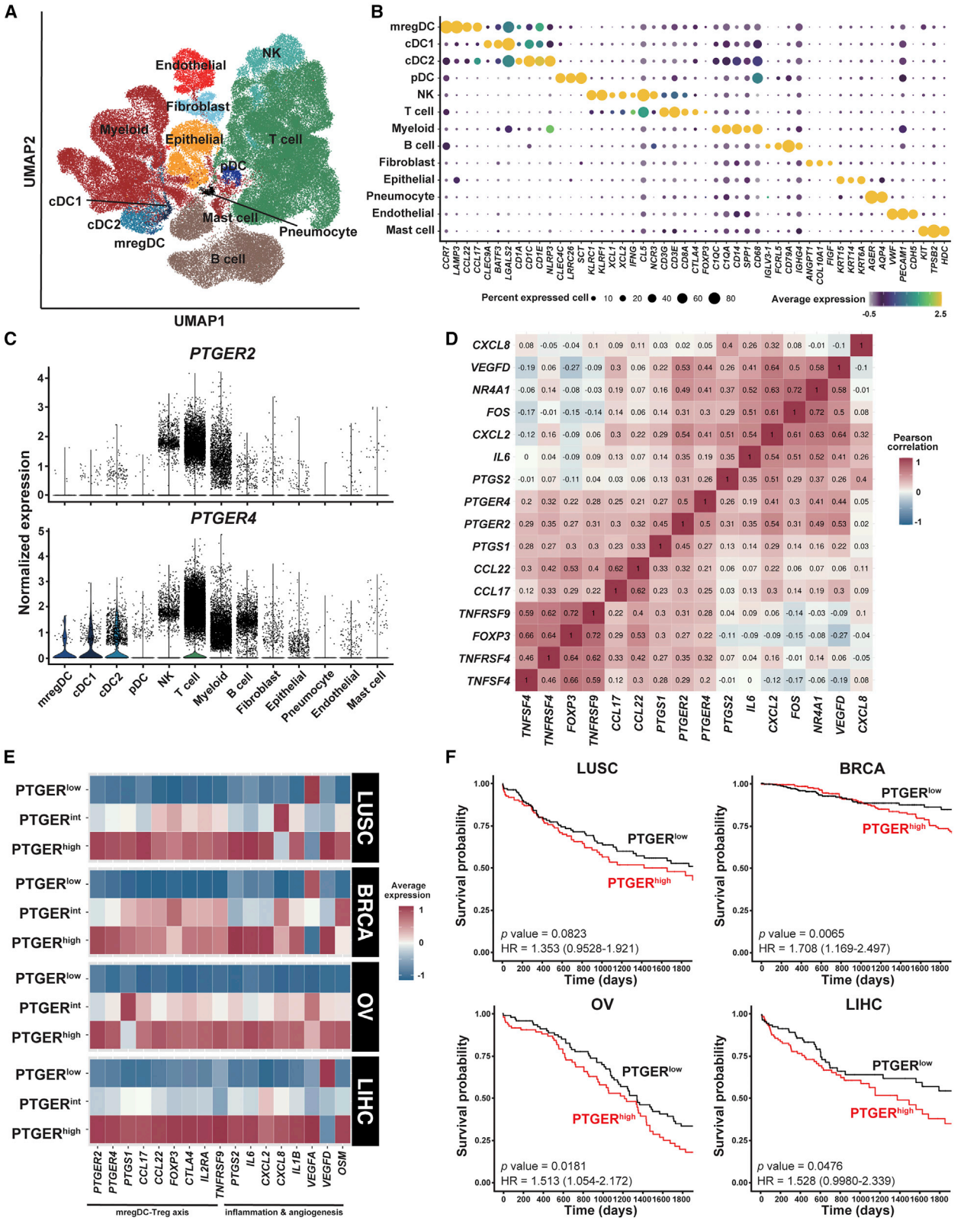

(legend on next page)

We then analyzed gene expression in Tregs subclustered from the tumor-infiltrating T cell population (Figures S4H and S4I). The expression of Treg signature genes *Foxp3*, *Stat5b*, *Il2ra*, *and Ctla4*, tended to be suppressed at the 1.5-day EP2/4i treatment (Figure S4J), and when compared on the fold change basis, the expression of these genes and genes highly expressed in tumor-infiltrating Tregs such as *Tnfrsf4*, *Tnfrsf9,* and *Tnfrsf18*, decreased further from 1.5 to 6 days upon EP2/4i treatment in a time-dependent manner (Figure S4K). These results together suggest that the suppression of Treg may occur slowly during EP2/4i treatment.

Finally, we conducted DEG analysis in integrated myeloid cells (TAN s1 and s2, Mono s1–s4, and TAM) of EP2/4i-treated (1.5-day) versus control mice and found an upregulation of a large number of ISGs (Figure S4L). This upregulation of ISGs was apparently stronger than what we observed at 6-day treatment (Figure S3Q), suggesting that IFN responses were rapidly induced by the EP2/4i treatment and reduced over time.

PTGER2/*PTGER4* expression correlates with gene expression signatures of the inflammatory myeloid cells and the immunosuppressive mregDC-Treg axis and has significant prognosis value in various human cancers

We next investigated whether and to what extent our findings from the LLC1 tumor model can be extrapolated to human tumors and have clinical implications. Since LLC1 is of lung squamous cell cancer (LUSC) origin, we analyzed the publicly available scRNA-seq dataset of human LUSC (Maier et al., 2020). Using the same pre-processing and quality control as the mouse scRNA-seq, we obtained a total of 89,000 cells from 12 tumor samples from 5 LUSC patients. Unsupervised clustering of the integrated scRNA-seq data gave rise to 13 clusters (Figure 5A). We identified the cell types according to the gene signatures, which comprise 4 subpopulations of DCs (cDC1s, cDC2s, mregDCs, and pDCs), populations for NK cells, T cells, myeloid cells, B cells, fibroblasts, epithelial cells, pneumocytes, endothelial cells, and mast cells (Figure 5B). When compared with the LLC1 tumors, the tumor-infiltrating T cells were relatively abundant and there were fewer myeloid cells in the human LUSC dataset, whereas the proportions of DC subpopulations in $CD45^+$ cells were similar to those found in the mouse LLC1 tumor (Figure S5A). Violin plots showed the expression of both *PTGER2* and *PTGER4* in a fraction of myeloid cells, T cells, and NK cells and relatively high expression of *PTGER4* in mregDC, cDC1, and cDC2 in LUSC (Figure 5C), as seen in the LLC1 mouse tumor (Figure 2F). Moreover, similar to the LLC1 tumor, active inflammation-related genes, including *PTGS2*, *IL1B*, *VEGFA*, *and HIF1A*, were dominantly expressed by myeloid cells (Figure S5B), and those genes involved in the recruitment and activation of tumor-infiltrating Tregs, including *CCL17* and *CCL22*, were highly expressed in mregDCs (Figure 5B).

We next used the TCGA datasets and conducted expression correlation analyses between genes in the COX-EP2/EP4 pathway and the genes involved in the two mechanisms (i.e., active inflammation and Treg recruitment and activation in human cancers). We chose 549 LUSC patients whose RNA-seq data were available out of the total of 765 cases, and extracted the genes that showed significant correlation with the expression of *PTGS1* or *PTGS2* (Tables S4 and S5). Interestingly, the expression of several proinflammatory/angiogenesis-related genes such as *CXCL8*, *VEGFD*, *NR4A1*, *FOS*, *CXCL2*, and *IL6* were highly correlated with that of *PTGS2*, whereas the expression of several genes involved in Treg recruitment and activation such as *CCL22*, *CCL17*, *TNFRSF9*, *FOXP3*, *TNFRSF4*, and *TNFSF4* were highly correlated with that of *PTGS1* (Figures 5D, S5C, and S5D). Notably, *PTGER2* and *PTGER4* expression is highly correlated with both *PTGS1* and *PTGS2* modules (Figure 5D). We next calculated the average expression of *PTGER2* and *PTGER4* (referred here as "PTGER score") and found that the genes of both *PTGS1* and *PTGS2* modules described above were highly correlated with high PTGER score in not only LUSC but also breast invasive carcinoma (BRCA), ovarian serous cystadenocarcinoma (OV), and liver hepatocellular carcinoma (LIHC) (Figure 5E). Moreover, a high PTGER score was significantly associated with the lower overall survival of BRCA, OV, and LIHC patients and a similar trend was observed in LUSC (Figure 5F). These results together suggest that *PTGER2* and *PTGER4* expression levels are correlated with the expression levels of genes related to active inflammation in myeloid cells and immunosuppression in mregDC-Treg, and have a prognosis value in various human cancers.

DISCUSSION

The discovery of immune checkpoint mechanisms and ICIs has revolutionized cancer therapeutics and provided a proof-of-principle of the strategy to harness the immune system to combat cancer (Sharma and Allison, 2020; Chamoto et al., 2020). However, while ICI is an effective cancer therapeutic, only a fraction of cancer patients, typically less than 40% in several types of cancer, showed a response, which led to the proposal of ICI resistance in unresponsive patients (Pitt et al., 2016). One

Figure 5. Association of *PTGER2* and *PTGER4* expression with the "inflammatory-angiogenic" and "mregDC-Treg" signatures and patient outcomes

(A) UMAP plot of cells obtained from 12 samples of 5 LUSC patients (89,000 cells) (from scRNA-seq analysis of LUSC patient cohort, Maier et al., 2020).

(B) Dot plot showing the expression of discriminatory markers for each cell population in (A).

(C) Violin plots based on scRNA-seq analysis showing the gene expression distribution of *PTGER2* and *PTGER4* in each identified cell type.

(D) Correlation plot of selected genes that show significant correlation with *PTGS1* and/or *PTGS2* expression in a TCGA human LUSC cohort (n = 542).

(E) Heatmap showed the expression level of representative genes involved in Treg recruitment and activation and in inflammation/angiogenesis in LUSC (n = 542), BRCA (n = 1,194), OV (n = 378), and LIHC (n = 418) patients. Patients were stratified into 3 groups ($PTGER^{high}$, $PTGER^{int}$, $PTGER^{low}$) based on PTGER score (mean expression of *PTGER2* and *PTGER4*).

(F) The Kaplan-Meier overall survival curve of LUSC (n = 542), BRCA (n = 1,194), OV (n = 378), and LIHC (n = 418) patients in TCGA datasets grouped by PTGER score. Hazard ratio (HR) for overall survival and its 95% confidence interval are shown. p value was calculated by multivariate Cox regression.

proposed mechanism underlying such ICI resistance and sensitivity is the "non-inflamed" versus "flamed" TME, and targeting to innate sensing, for example, is suggested to convert "non-inflamed" to "inflamed" TME to overcome the ICI resistance (Liu et al., 2020). However, "inflamed" TME does not always overcome ICI resistance because active inflammation often occurs in parallel with immunosuppression in TME. This raises a question as to why inflammation does not lead to immune activation in TME (Greten and Grivennikov, 2019; Shalapour and Karin, 2019). In this study, we tackled this question by examining the actions of PGE_2 in the ICI-insensitive LLC1 mouse tumor. To obtain the cellular and molecular landscape shaped by the PGE_2-EP2/4 signaling in TME, we combined pharmacological intervention and scRNA-seq analysis, so that molecular changes associated with EP2/EP4 inhibition can be detected at the single-cell resolution at different time points. Using this approach, we discovered two major actions that PGE_2-EP2/4 signaling elicits there. One is the promotion of active inflammation through the upregulation of NF-κB signaling in myeloid cells and the other is the immunosuppression through the mregDC-Treg axis. Thus, PGE_2-EP2/EP4 signaling functions as a regulatory node in TME to control both inflammation and immunosuppression.

In LLC1 TME, we found the expression of a variety of NF-κB-target proinflammatory-angiogenesis genes such as *Ptgs2*, *Il1b*, *Cxcl2*, *Vegfa*, and *Hif1a* genes in a wide range of myeloid cell populations from TAN and Mono to TAM, and that this expression was rapidly and markedly inhibited with the blockade of EP2/EP4. Moreover, we found that EP2/EP4 inhibition reduced the expression of genes of NF-κB complex components such as *Rela*, *Nfkb1*, and *Nfkbiz* in the above wide range of myeloid cells (Figure 3C). Our finding therefore indicates that in the context of LLC1 tumors, PGE_2-EP2/EP4 signaling shapes active inflammatory TME by upregulating NF-κB signaling and has thus provided an answer to one of the important questions in cancer biology: How is NF-κB activation regulated in TME? (Taniguchi and Karin, 2018). Notably, of the myeloid cells, the strongest suppression of inflammatory and angiogenesis genes by EP2/4i was observed in the TAN population. Given that TAN is the only tumor-infiltrating immune cell population that was significantly decreased upon EP2/4i treatment, it is likely that TAN is particularly sensitive to EP2/4i blocking. The mechanism underlying this sensitivity remains to be clarified by further investigation.

More important, we have discovered here that the PGE_2-EP2/EP4 signaling drives the mregDC-Treg axis and elicits immunosuppression in TME. mregDC is a recently identified novel DC state that has the potential to generate both immunostimulatory and immunoregulatory molecules (Maier et al., 2020). Given that other DCs are generally immune-activating cells, the potential to produce immunoregulatory molecules is unique to mregDCs. Using scRNA-seq, we found mregDC to be the *Ccr7*-expressing DC cell population that expresses the highest level of EP4 and produces the highest amount of Ccl17 and Ccl22 among the tumor-infiltrating immune cells. Intriguingly, the inhibition of EP2 and EP4 rapidly and strongly reduced the production of these chemokines. Moreover, the neutralization of Ccl22 and Ccl17 resulted in the reduction of tumor-infiltrating Tregs. Consistently, EP2/4 inhibition also decreased the number of tumor-infiltrating Tregs. These results together suggest that PGE_2-EP2/EP4 signaling exerts its function on mregDCs to produce Ccl22 and Ccl17, which recruit Tregs to tumor sites. Interestingly, PGE_2-EP2/EP4 signaling is involved not only in the recruitment of Treg to the tumor but also their activation. We found that Tregs in LLC1 TME express genes involved in their own activation, including the master regulator *Foxp3*, critical signaling molecules such as *Il2ra* and *Stat5b*, and coactivators *Tnfrsf4*, *Tnfrsf9*, and *Tnfrsf18*, and that the EP2/EP4 inhibition gradually downregulated the expression of all of these genes. It should be noted that the expression of these co-activator molecules has been reported as a hallmark of tumor-infiltrating Tregs (Freeman et al., 2020). These co-activator molecules induced in Tregs may be involved in further Treg activation by binding to their ligands presented by other tumor-infiltrating immune cells.

Intriguingly, our scRNA-seq analysis showed a marked enhancement of ISGs expression associated with Treg depletion, indicating that antitumor activity upon Treg depletion/attenuation in LLC1 tumors is not only mediated by $CD4^+$ and $CD8^+$ T cells but also type I IFN. Interestingly, EP2/4i treatment also induced ISGs expression in various cell types in LLC1 tumors (Figure S3Q), and this action was particularly strong at the early time point (Figure S4L). Given a previous report that PGE_2 could suppress type I IFN production by myeloid cells via EP2 and EP4 in an influenza A infection mouse model (Coulombe et al., 2014), these results together suggest a possibility that EP2/EP4 signaling suppresses IFN release both directly and indirectly through Tregs. Given the antitumor activity of type I IFN (Borden, 2019), these results suggest that EP2/EP4 blockade may also provide some benefits by type I IFN release. Thus, PGE_2-EP2/EP4 signaling elicits its function in TME by the promotion of active inflammation mediated by myeloid cells and immunosuppression mediated by mregDC-Treg axis together with inhibition of type I IFN production. This integration by PGE_2 is critical in TME because inflammation alone can favor immune activation and cancer-inhibitory effects (Mantovani et al., 2008; Vesely et al., 2011; Coussens et al., 2013).

Finally, and most importantly, our analysis of the published scRNA-seq datasets of human LUSC patients and the TCGA datasets showed that the expression of genes in the PGE_2-EP2/EP4 signaling, *PTGS1*, *PTGS2*, *PTGER2*, and *PTGER4*, are strongly correlated with the expression of genes of the two signatures we found in LLC1 tumors (i.e., proinflammatory/angiogenesis myeloid cells and immunosuppressive mregDC-Tregs) in various human tumors, and demonstrated that the expression of *PTGER2* and *PTGER4* together correlates negatively with patient prognosis in LUSC, BRCA, LIHC, and OV, suggesting that the action mechanisms of PGE_2-EP2/EP4 signaling that we found here are conserved and critically function in human cancers. Ever since the epidemiological finding that aspirin use lowers the risk of cancer death, the use of NSAIDs as chemopreventive and therapeutic agents for cancer has been tested repeatedly. However, the gastrointestinal toxicity associated with general NSAIDs and the cardiovascular toxicity of COX2 inhibitors have hampered their extensive use, which has led to the suggestion of manipulation of downstream PG signaling as an alternative measure. Currently, several EP4 antagonists and an EP2/EP4 dual antagonist are under investigation in clinical trials for different solid cancers (NCT04344795, NCT02540291,

NCT03152370, NCT04432857, NCT03155061, NCT03661632, NCT03658772, and NCT02538432) (Hong et al., 2020; Thumkeo and Narumiya, 2021). Given the advances in our understanding of the PGE_2-EP2/EP4 signaling actions in TME as exemplified by the present study, it is now the time to exploit such findings and explore the clinical utility of EP2/EP4 antagonists based on the TME landscape that the PGE_2-EP2/EP4 signaling shapes in each clinical cancer.

Limitations of the study

One limitation of this study is the use of a single syngeneic tumor model, LLC1, in C57BL/6 mice. This study therefore cannot exclude the operation of the EP2/EP4-dependent mechanisms reported in other models such as the inhibition of the NK cells-cDC1 axis (Zelenay et al., 2015; Bottcher et al., 2018; Bonavita et al., 2020), as well as other EP2/EP4-dependent mechanisms in T cell-enriched TME. In addition, we used only fixed doses of the EP2 and EP4 antagonists and examined their responses in this study. It is therefore unclear that some findings such as insufficient activation of $CD4^+$ and $CD8^+$ T cells with EP2/4i were due to inefficient EP2/EP4 inhibition or the presence of redundant mechanisms. Also, since we focused the actions of EP2/EP4 signaling in $CD45^+$ immune cells, we have addressed neither the role of this signaling in stromal cells nor the roles of EP1 or EP3 receptors expressed at low and intermediate levels, respectively, in both $CD45^+$ and $CD45^-$ cells in LLC1 tumors.

STAR★METHODS

Detailed methods are provided in the online version of this paper and include the following:

- KEY RESOURCES TABLE
- RESOURCE AVAILABILITY
  - Lead contact
  - Materials availability
  - Data and code availability
- EXPERIMENTAL MODEL AND SUBJECT DETAILS
  - Tumor cell line
  - Animal model
- METHOD DETAILS
  - Synthesis of AS3385282-00
  - Measurement of NMR and mass spectra of AS3385282-00
  - cAMP assay
  - Effect of AS3385282-00 on EP2 agonist-mediated blood pressure elevation in mouse
  - Cell viability assay
  - Tumor cell injections and tumor growth experiments
  - Mouse tumor tissue digestion
  - Single-cell RNA sequencing (scRNA-seq)
  - Single-cell data processing
  - Quality control, cellular identification and clustering analysis
  - FACS analysis
  - ELISA assay for Ccl22 and Ccl17 measurement in sort-purified $Ccr7^+$ cDC, cDC2, CD45(−) cell and TAM from LLC1 tumor
  - Treg *in vitro* culture assays
  - Quantitative RT-PCR analysis
  - Drug administration and anti-PD-1 antibody treatment
  - Treg depletion and depletion of CD8 T cells
  - Ccl17 and Ccl22 neutralization
  - Histology and immunohistochemistry
  - Bioinformatics analysis of TCGA database
- QUANTIFICATION AND STATISTICAL ANALYSIS
  - Quantitative analysis of blood vessels density
  - Statistical analyses

SUPPLEMENTAL INFORMATION

Supplemental information can be found online at https://doi.org/10.1016/j.celrep.2022.110914.

ACKNOWLEDGMENTS

We thank A. Watanabe for supporting the scRNA-seq experiments; N. Mikami for advice on *in vitro* iTreg experiment; K. Hanaoka, H. Tanaka, K. Naruo, T. Kurita, A. Washio, and Y. Yoshii for technical assistance; and T. Arai for secretarial assistance. The super-computing resource "SHIROKANE" was provided by the Human Genome Center, University of Tokyo (http://sc.hgc.jp/shirokane.html). The graphical abstract was created by BioRender. This work was supported in part by Grants-in-Aid for Scientific Research from the Ministry of Education, Culture, Sports, Science, and Technology of Japan (to D.T. and S.N.), a research grant from the Ono Medical Research Foundation (to D.T.), a research grant from the Shimizu Foundation for Immunology and Neuroscience (to D.T.), a research grant from the Kyoto Preventive Medical Center (to D.T.), and the Special Coordination Funds by the Ministry of Education, Culture, Sports, Science, and Technology of Japan and Astellas Pharma in the Creation of Innovation Centers for Advanced Interdisciplinary Research Areas (to D.T. and S.N.). D.T. and S.N. were supported by the Coordination Fund from JST and Astellas Pharma.

AUTHOR CONTRIBUTIONS

D.T. and S.N. designed the research. D.T., S. Prasongtanakij, R.M., K.A., H.N., and R.Y. performed the experiments. N.A. and H.H. synthesized and characterized AS3385282-00. S. Sugahara and S.T. conducted the cAMP assay. S. Punyawatthananukool and D.T. conducted the mouse scRNA-seq and data analysis. S. Punyawatthananukool and D.T. conducted TCGA database and public human scRNA-seq data analysis. D.T. and S. Punyawatthananukool performed the statistical analysis. V.C. supervised the scRNA-seq data analysis. A.T. and S. Sakaguchi provided the necessary research materials and supervised the Treg analysis. D.T., S. Punyawatthananukool, and S.N. wrote the manuscript. All of the authors reviewed and approved the manuscript.

DECLARATION OF INTERESTS

S.N. is a scientific advisor to Astellas Pharma and Toray. R.Y., N.A., H.H., S. Sugahara, and S.T. are employees of Astellas Pharma.

Received: June 21, 2021
Revised: February 11, 2022
Accepted: May 11, 2022
Published: June 7, 2022

REFERENCES

Albu, D.I., Wang, Z., Huang, K.C., Wu, J., Twine, N., Leacu, S., Ingersoll, C., Parent, L., Lee, W., Liu, D., et al. (2017). EP4 Antagonism by E7046 diminishes myeloid immunosuppression and synergizes with Treg-reducing IL-2-Diphtheria toxin fusion protein in restoring anti-tumor immunity. OncoImmunology *6*, e1338239. https://doi.org/10.1080/2162402x.2017.1338239.

Andrews, S. (2010). FastQC: A Quality Control Tool for High Throughput Sequence Data. http://www.bioinformatics.babraham.ac.uk/projects/fastqc.

Becker, D.P., Villamil, C.I., Barta, T.E., Bedell, L.J., Boehm, T.L., DeCrescenzo, G.A., Freskos, J.N., Getman, D.P., Hockerman, S., Heintz, R., et al. (2005). Synthesis and structure- activity relationships of β- and α-piperidine sulfone hydoxamic acid matrix metalloproteinase inhibitors with oral antitumor efficacy. J. Med. Chem. *48*, 6713–6730. https://doi.org/10.1021/jm0500875.

Bonavita, E., Bromley, C.P., Jonsson, G., Pelly, V.S., Sahoo, S., Walwyn-Brown, K., Mensurado, S., Moeini, A., Flanagan, E., Bell, C.R., et al. (2020). Antagonistic inflammatory phenotypes dictate tumor fate and response to immune checkpoint blockade. Immunity *53*, 1215–1229.e8. https://doi.org/10.1016/j.immuni.2020.10.020.

Borden, E.C. (2019). Interferons alpha and beta in cancer: therapeutic opportunities from new insights. Nat. Rev. Drug Discov. *18*, 219–234. https://doi.org/10.1038/s41573-018-0011-2.

Bottcher, J.P., Bonavita, E., Chakravarty, P., Blees, H., Cabeza-Cabrerizo, M., Sammicheli, S., Rogers, N.C., Sahai, E., Zelenay, S., and Reis e Sousa, C. (2018). NK cells stimulate recruitment of cDC1 into the tumor microenvironment promoting cancer immune control. Cell *172*, 1022–1037.e14. https://doi.org/10.1016/j.cell.2018.01.004.

Chamoto, K., Hatae, R., and Honjo, T. (2020). Current issues and perspectives in PD-1 blockade cancer immunotherapy. Int. J. Clin. Oncol. *25*, 790–800. https://doi.org/10.1007/s10147-019-01588-7.

Chen, D.S., and Mellman, I. (2017). Elements of cancer immunity and the cancer-immune set point. Nature *541*, 321–330. https://doi.org/10.1038/nature21349.

Coulombe, F., Jaworska, J., Verway, M., Tzelepis, F., Massoud, A., Gillard, J., Wong, G., Kobinger, G., Xing, Z., Couture, C., et al. (2014). Targeted prostaglandin E2 inhibition enhances antiviral immunity through induction of type I interferon and apoptosis in macrophages. Immunity *40*, 554–568. https://doi.org/10.1016/j.immuni.2014.02.013.

Coussens, L.M., Zitvogel, L., and Palucka, A.K. (2013). Neutralizing tumor-promoting chronic inflammation: a magic bullet? Science *339*, 286–291. https://doi.org/10.1126/science.1232227.

Freeman, Z.T., Nirschl, T.R., Hovelson, D.H., Johnston, R.J., Engelhardt, J.J., Selby, M.J., Kochel, C.M., Lan, R.Y., Zhai, J., Ghasemzadeh, A., et al. (2020). A conserved intratumoral regulatory T cell signature identifies 4-1BB as a pan-cancer target. J. Clin. Invest. *130*, 1405–1416. https://doi.org/10.1172/jci128672.

Giovanelli, P., Sandoval, T.A., and Cubillos-Ruiz, J.R. (2019). Dendritic cell metabolism and function in tumors. Trends Immunol. *40*, 699–718. https://doi.org/10.1016/j.it.2019.06.004.

Greten, F.R., and Grivennikov, S.I. (2019). Inflammation and cancer: triggers, mechanisms, and consequences. Immunity *51*, 27–41. https://doi.org/10.1016/j.immuni.2019.06.025.

Hafemeister, C., and Satija, R. (2019). Normalization and variance stabilization of single cell RNA-seq data using regularized negative binomial regression. Genome Biol. *20*, 296. https://doi.org/10.1186/s13059-019-1874-1.

Hizaki, H., Segi, E., Sugimoto, Y., Hirose, M., Saji, T., Ushikubi, F., Matsuoka, T., Noda, Y., Tanaka, T., Yoshida, N., et al. (1999). Abortive expansion of the cumulus and impaired fertility in mice lacking the prostaglandin E receptor subtype EP(2). Proc. Natl. Acad. Sci. U S A *96*, 10501–10506. https://doi.org/10.1073/pnas.96.18.10501.

Hong, D.S., Parikh, A., Shapiro, G.I., Varga, A., Naing, A., Meric-Bernstam, F., Ataman, O., Reyderman, L., Binder, T.A., Ren, M., et al. (2020). First-in-human phase I study of immunomodulatory E7046, an antagonist of PGE2-receptor E-type 4 (EP4), in patients with advanced cancers. J Immunother. Cancer *8*, e000222. https://doi.org/10.1136/jitc-2019-000222.

Johnson, A.M., Kleczko, E.K., and Nemenoff, R.A. (2020). Eicosanoids in cancer: new roles in immunoregulation. Front. Pharmacol. *11*, 595498. https://doi.org/10.3389/fphar.2020.595498.

Kim, J.M., Rasmussen, J.P., and Rudensky, A.Y. (2007). Regulatory T cells prevent catastrophic autoimmunity throughout the lifespan of mice. Nat. Immunol. *8*, 191–197. https://doi.org/10.1038/ni1428.

Lee, J., Aoki, T., Thumkeo, D., Siriwach, R., Yao, C., and Narumiya, S. (2019). T cell-intrinsic prostaglandin E2-EP2/EP4 signaling is critical in pathogenic TH17 cell-driven inflammation. J. Allergy Clin. Immunol. *143*, 631–643. https://doi.org/10.1016/j.jaci.2018.05.036.

Liu, L., Ge, D., Ma, L., Mei, J., Liu, S., Zhang, Q., Ren, F., Liao, H., Pu, Q., Wang, T., and You, Z. (2012a). Interleukin-17 and Prostaglandin E2 are involved in formation of an M2 Macrophage-dominant microenvironment in lung cancer. J. Thorac. Oncol. *7*, 1091–1100. https://doi.org/10.1097/jto.0b013e3182542752.

Liu, S.Y., Sanchez, D.J., Aliyari, R., Lu, S., and Cheng, G. (2012b). Systematic identification of type I and type II interferon-induced antiviral factors. Proc. Natl. Acad. Sci. U S A *109*, 4239–4244. https://doi.org/10.1073/pnas.1114981109.

Liu, Z., Han, C., and Fu, Y.-X. (2020). Targeting innate sensing in the tumor microenvironment to improve immunotherapy. Cell. Mol. Immunol. *17*, 13–26. https://doi.org/10.1038/s41423-019-0341-y.

Lu, W., Yu, W., He, J., Liu, W., Yang, J., Lin, X., Zhang, Y., Wang, X., Jiang, W., Luo, J., et al. (2021). Reprogramming immunosuppressive myeloid cells facilitates immunotherapy for colorectal cancer. EMBO Mol. Med. *13*, e12798. https://doi.org/10.15252/emmm.202012798.

Maier, B., Leader, A.M., Chen, S.T., Tung, N., Chang, C., LeBerichel, J., Chudnovskiy, A., Maskey, S., Walker, L., Finnigan, J.P., et al. (2020). A conserved dendritic-cell regulatory program limits antitumour immunity. Nature *580*, 257–262. https://doi.org/10.1038/s41586-020-2134-y.

Mantovani, A., Allavena, P., Sica, A., and Balkwill, F. (2008). Cancer-related inflammation. Nature *454*, 436–444. https://doi.org/10.1038/nature07205.

Mikami, N., Kawakami, R., Chen, K.Y., Sugimoto, A., Ohkura, N., and Sakaguchi, S. (2020). Epigenetic conversion of conventional T cells into regulatory T cells by CD28 signal deprivation. Proc. Natl. Acad. Sci. U S A *117*, 12258–12268. https://doi.org/10.1073/pnas.1922600117.

Mizukami, K., Kamada, H., Yoshida, H., Ishii, I., Nozawa, E., Wada, K., and Ugawa, T. (2018). Pharmacological properties of ASP7657, a novel, potent, and selective prostaglandin EP4 receptor antagonist. Naunyn-Schmiedeberg. Arch. Pharmacol. *391*, 1319–1326. https://doi.org/10.1007/s00210-018-1545-x.

Palucka, A.K., and Coussens, L.M. (2016). The basis of oncoimmunology. Cell *164*, 1233–1247. https://doi.org/10.1016/j.cell.2016.01.049.

Pahl, H.L. (1999). Activators and target genes of Rel/NF-κB transcription factors. Oncogene *18*, 6853–6866. https://doi.org/10.1038/sj.onc.1203239.

Pitt, J.M., Vetizou, M., Daillere, R., Roberti, M.P., Yamazaki, T., Routy, B., Lepage, P., Boneca, I.G., Chamaillard, M., Kroemer, G., and Zitvogel, L. (2016). Resistance mechanisms to immune-checkpoint blockade in cancer: tumor-intrinsic and -extrinsic factors. Immunity *44*, 1255–1269. https://doi.org/10.1016/j.immuni.2016.06.001.

R Core Team (2014). R: A Language and Environment for Statistical Computing (R Foundation for Statistical Computing). http://www.R-project.org/.

Rigas, B., Goldman, I.S., and Levine, L. (1993). Altered eicosanoid levels in human colon cancer. J. Lab. Clin. Med. *122*, 518–523.

Sakaguchi, S., Mikami, N., Wing, J.B., Tanaka, A., Ichiyama, K., and Ohkura, N. (2020). Regulatory T cells and human disease. Annu. Rev. Immunol. *38*, 541–566. https://doi.org/10.1146/annurev-immunol-042718-041717.

Schneider, A., Guan, Y., Zhang, Y., Magnuson, M.A., Pettepher, C., Loftin, C.D., Langenbach, R., Breyer, R.M., and Breyer, M.D. (2004). Generation of a conditional allele of the mouse prostaglandin EP4 receptor. Genesis *40*, 7–14. https://doi.org/10.1002/gene.20048.

Shalapour, S., and Karin, M. (2019). Pas de Deux: control of anti-tumor immunity by cancer-associated inflammation. Immunity *51*, 15–26. https://doi.org/10.1016/j.immuni.2019.06.021.

Sharma, P., and Allison, J.P. (2020). Dissecting the mechanisms of immune checkpoint therapy. Nat. Rev. Immunol. *20*, 75–76. https://doi.org/10.1038/s41577-020-0275-8.

Sinha, P., Clements, V.K., Fulton, A.M., and Ostrand-Rosenberg, S. (2007). Prostaglandin E2 promotes tumor progression by inducing myeloid-derived suppressor cells. Cancer Res. *67*, 4507–4513. https://doi.org/10.1158/0008-5472.can-06-4174.

Stuart, T., Butler, A., Hoffman, P., Hafemeister, C., Papalexi, E., Mauck, W.M., 3rd, Hao, Y., Stoeckius, M., Smibert, P., and Satija, R. (2019). Comprehensive integration of single-cell data. Cell *177*, 1888–1902.e21. https://doi.org/10.1016/j.cell.2019.05.031.

Subramanian, A., Tamayo, P., Mootha, V.K., Mukherjee, S., Ebert, B.L., Gillette, M.A., Paulovich, A., Pomeroy, S.L., Golub, T.R., Lander, E.S., and Mesirov, J.P. (2005). Gene set enrichment analysis: a knowledge-based approach for interpreting genome-wide expression profiles. Proc. Natl. Acad. Sci. U S A *102*, 15545–15550. https://doi.org/10.1073/pnas.0506580102.

Sugimoto, Y., and Narumiya, S. (2007). Prostaglandin E receptors. J. Biol. Chem. *282*, 11613–11617. https://doi.org/10.1074/jbc.r600038200.

Taniguchi, K., and Karin, M. (2018). NF-κB, inflammation, immunity and cancer: coming of age. Nat. Rev. Immunol. *18*, 309–324. https://doi.org/10.1038/nri.2017.142.

Thumkeo, D., and Narumiya, S. (2021). Opening the door to better aspirin. Structure *29*, 200–202. https://doi.org/10.1016/j.str.2021.02.003.

Vasse, M., Pourtau, J., Trochon, V., Muraine, M., Vannier, J.P., Lu, H., Soria, J., and Soria, C. (1999). Oncostatin M induces angiogenesis in vitro and in vivo. Arterioscler. Thromb. Vasc. Biol. *19*, 1835–1842. https://doi.org/10.1161/01.atv.19.8.1835.

Vesely, M.D., Kershaw, M.H., Schreiber, R.D., and Smyth, M.J. (2011). Natural innate and adaptive immunity to cancer. Annu. Rev. Immunol. *29*, 235–271. https://doi.org/10.1146/annurev-immunol-031210-101324.

Wang, D., and Dubois, R.N. (2010). Eicosanoids and cancer. Nat. Rev. Cancer *10*, 181–193. https://doi.org/10.1038/nrc2809.

Wang, D., and DuBois, R.N. (2015). Immunosuppression associated with chronic inflammation in the tumor microenvironment. Carcinogenesis *36*, 1085–1093. https://doi.org/10.1093/carcin/bgv123.

Wculek, S.K., Cueto, F.J., Mujal, A.M., Melero, I., Krummel, M.F., and Sancho, D. (2020). Dendritic cells in cancer immunology and immunotherapy. Nat. Rev. Immunol. *20*, 7–24. https://doi.org/10.1038/s41577-019-0210-z.

Wickham, H. (2009). ggplot2: Elegant Graphics for Data Analysis (Springer-Verlag).

Yang, L., Yamagata, N., Yadav, R., Brandon, S., Courtney, R.L., Morrow, J.D., Shyr, Y., Boothby, M., Joyce, S., Carbone, D.P., and Breyer, R.M. (2003). Cancer-associated immunodeficiency and dendritic cell abnormalities mediated by the prostaglandin EP2 receptor. J. Clin. Invest. *111*, 727–735. https://doi.org/10.1172/jci16492.

Yang, S., Corbett, S.E., Koga, Y., Wang, Z., Johnson, W.E., Yajima, M., and Campbell, J.D. (2020). Decontamination of ambient RNA in single-cell RNA-seq with DecontX. Genome Biol. *21*, 57. https://doi.org/10.1186/s13059-020-1950-6.

Yang, Y., Wu, J., and Wang, J. (2016). A database and functional annotation of NF-κB target genes. Int. J. Clin. Exp. Med. *9*, 7986–7995.

Yoshie, O., and Matsushima, K. (2015). CCR4 and its ligands: from bench to bedside. Int. Immunol. *27*, 11–20. https://doi.org/10.1093/intimm/dxu079.

Yu, G., Wang, L.G., Han, Y., and He, Q.Y. (2012). clusterProfiler: an R package for comparing biological themes among gene clusters. OMICS *16*, 284–287. https://doi.org/10.1089/omi.2011.0118.

Yuan, H., Chen, P.W., Li, M.Y., Zhang, Y., Peng, Z.W., Liu, W., Paton, R.S., and Cao, C. (2020). Effects of substituents X and Y on the NMR chemical shifts of 2-(4-X phenyl)-5-Y pyrimidines. J. Mol. Struct. *1204*, 127489. https://doi.org/10.1016/j.molstruc.2019.127489.

Zelenay, S., van der Veen, A.G., Bottcher, J.P., Snelgrove, K.J., Rogers, N., Acton, S.E., Chakravarty, P., Girotti, M.R., Marais, R., Quezada, S.A., et al. (2015). Cyclooxygenase-dependent tumor growth through evasion of immunity. Cell *162*, 1257–1270. https://doi.org/10.1016/j.cell.2015.08.015.

STAR★METHODS

KEY RESOURCES TABLE

REAGENT or RESOURCE	SOURCE	IDENTIFIER
Antibodies		
IgG2b isotype control anti-mouse (LTF-2)	BioXcell	RRID: AB_1107780
Anti-mouse CD8a (2.43)	BioXcell	RRID: AB_1125541
Anti-mouse PD-1 (RMP1-14)	BioXcell	RRID: AB_10949053
Rat IgG2a isotype control (2A3)	BioXcell	RRID: AB_1107769
APC anti-mouse Ly6C	Biolegend	RRID: AB_1732076
APC anti-mouse CD11c	eBioscience	RRID: AB_469346
APC anti-mouse Foxp3	eBioscience	RRID: AB_469457
APC anti-mouse CD45	Biolegend	RRID: AB_312977
APC/Cyanine7 anti-mouse CD3	Biolegend	RRID: AB_2242784
APC/Cyanine7 anti-mouse NK-1.1	Biolegend	RRID: AB_830871
APC/Cyanine7 anti-mouse Ly6C	Biolegend	RRID: AB_10640120
APC/Cyanine7 anti-mouse F4/80	Biolegend	RRID: AB_893489
BV510 Rat anti-mouse CD8a	BD Horizon	RRID: AB_2687548
BV510 Rat anti-mouse/human CD11b	BD Horizon	RRID: AB_2737913
BV510 Rat anti-mouse CD45	Biolegend	RRID: AB_2563061
FITC anti-mouse CD4	Biolegend	RRID: AB_312713
FITC anti-mouse Ly6G	Biolegend	RRID: AB_1236494
FITC anti-mouse CD45	eBioscience	RRID: AB_465050
FITC Rat anti-mouse CD11b	BD Pharmingen	RRID: AB_394774
PE anti-mouse CD335 (NKp46)	eBioscience	RRID: AB_1210743
PE anti-mouse F4/80	eBioscience	RRID: AB_465923
APC/Cyanine7 anti-mouse Ly6G	Biolegend	RRID: AB_10640819
PE anti-mouse I-A/I-E	Biolegend	RRID: AB_313323
PE anti-mouse CD8a	Biolegend	RRID: AB_312747
PE anti-mouse CD25	eBioscience	RRID: AB_10117160
PE-Texas Red anti-mouse CD45	Thermo Fisher	RRID: AB_10392557
PE-Cyanine7 anti-mouse CD137 (4-1bb)	eBioscience	RRID: AB_2573398
PerCP/Cyanine5.5 anti-mouse/human CD11b	Biolegend	RRID: AB_893232
PerCP/Cyanine5.5 anti-mouse Ly6G	Biolegend	RRID: AB_1877272
PerCP/Cyanine5.5 anti-mouse CD4	eBioscience	RRID: AB_1107001
PerCP/Cyanine5.5 anti-mouse CD197 (Ccr7)	Biolegend	RRID: AB_2291144
Pacific Blue anti-mouse CD3	Biolegend	RRID: AB_493645
Mouse Ccl22/MDC antibody	R&D	RRID: AB_355360
Mouse Ccl17/TARC antibody	R&D	RRID: AB_355416
Normal Goat IgG control	R&D	RRID: AB_354267
Anti-CD3 antibody (clone 2C11)	eBioscience	RRID: AB_467051
Anti-CD28 antibody (clone 37.51)	eBioscience	RRID: AB_467192
APC anti-human/mouse Gzmb	Biolegend	RRID: AB_2687028
Anti-mouse CD31 antibody	Abcam	RRID: AB_726362
Anti-mouse CD16/CD32 (Fc Block)	BD Pharmingen	RRID: AB_394656
Chemicals, peptides, and recombinant proteins		
SC-560 (Cox1 inhibitor)	TCI	Cat# C3572
Celecoxib (Cox2 inhibitor)	Cayman	Cat# 10008672

(*Continued on next page*)

Continued

REAGENT or RESOURCE	SOURCE	IDENTIFIER
0.5% Methylcellulose	Wako	Cat# 133-17815
AS3385282-00 (EP2 antagonist)	This study	N/A
PF04418948	Tocris	Cat# 4818
$NaHCO_3$	Nacalai	Cat# 09655-25
Normal saline	Otsuka	Cat# K4L77
Distilled water	Otsuka	Cat# 7I88N
(2-Hydroxypropyl)-β-cyclodextrin	Sigma-Aldrich	Cat# 389145
Polyethylene glycol #600	Nacalai	Cat# 11572-35
Polyethylene glycol #400	Nacalai	Cat# 11571-45
Tween80	Nacalai	Cat# 35703-75
HCO-40	NIKKOL	Cat# 61788-85-0
1mol/L-Hydrochloric acid	Nacalai	Cat# 11677-75
ASP7657 (EP4 antagonist)	Mizukami et al., 2018	N/A
Tamoxifen	SIGMA	Cat# T5648-5G
TGF-β1	R&D Systems	Cat# 240-B-002
IL-2	Peprotech	Cat# 200-02
Lipopolysaccharide (LPS) from E.coli O157	Nacalai	Cat# 20389-04
Tumor dissociation kit, mouse	Miltenyi	Cat# 130-096-730
Red blood cell lysis solution, 10x	Miltenyi	Cat# 130-094-183
GentleMACS C tube	Miltenyi	Cat# 130-096-334
DMEM	Gibco	Cat# 11995-065
Fetal bovine serum	SIGMA	Cat# F7524
Penicillin-Streptomycin mixed solution	Nacalai	Cat# 26253-84
RPMI media	Sigma	Cat# R8758
Dulbecco's PBS(-)	Nissui	Cat# 05913
Albumin, from Bovine Serum	Sigma	Cat# A2153
TRIzol reagent	Ambion	Cat# 15596018
Chloroform	Nacalai	Cat# 08402-55
2-Propanol	Nacalai	Cat# 29113-95
Ethanol	Nacalai	Cat# 14712-05
10% Formalin neutral buffer solution	FUJIFILM	Cat# 062-01661
Foxp3 staining kit	eBioscience	Cat# 00-5523-00
Violet fluorescent reactive dye	Invitrogen	Cat# L34955
Fixable Viability Dye eFluor 780	eBioscience	Cat# 65-0865-14
Diphtheria toxin (from Corynebacterium Diphtheriae)	Sigma	Cat# D0564
PGE_2	Cayman	Cat# 14010
Indomethacin	Sigma-Aldrich	Cat# I7378-5G
IBMX	Enzo Life Sciences	Cat# BML-PD140-1000
EP2 agonist	#compound no. 936 of patent WO2009113600	N/A
Critical commercial assays		
Chromium™ Next GEM Chip G single cell kit	10x Genomics	PN-1000120
Chromium™ i7 multiplex kit	10x Genomics	PN-120262
Chromium™ Next GEM single cell 3' GEM, library & gel bead kit v3.1	10x Genomics	PN-1000121
Dako EnVision+ system-HRP labelled polymer anti-rabbit	Dako	K4003
Dako liquid DAB+ substrate chromogen system	Dako	K3468
LEGENDplex mouse macrophage/microglia panel	Biolegend	Cat# 740846
Naïve CD4 T cell isolation kit (mouse)	Miltenyi	Cat# 130-117-043
RNeasy Plus Micro kit	QIAGEN	Cat# 74034

(*Continued on next page*)

Continued		
REAGENT or RESOURCE	SOURCE	IDENTIFIER
ReverTra Ace qPCR RT master mix with gDNA Remover	Toyobo	Cat# FSQ-301
THUNDERBIRD SYBR qPCR Mix	Toyobo	Cat# QPS-201x5
cAMP-Gs Femto2 kit cAMP-Gs Femto2 kit	Cisbio	Cat# 62AM5PEB
CellTiter-Glo® 2.0 Cell Viability Assay	Promega	Cat# G9242
Deposited data		
scRNA-seq data	This paper	GEO: GSE169688
Algorithms and computer codes	This paper	https://github.com/SiwakornP/scRNAseq_LLC1_EP2iEP4i
Raw quantification data and original images	This paper	Mendeley Data: https://doi.org/10.17632/b8kftkzvmd.1
Experimental models: Cell lines		
Mouse: LLC1	ATCC	Cat# CRL-1642
Experimental models: Mice		
C57BL/6N	SLC	N/A
UBC-CreERT2	Jackson Lab	Cat# 007001
EP2 KO	Hizaki et al., 1999	N/A
EP4 floxed	Schneider et al., 2004	N/A
EP2/4 double floxed	Lee et al., 2019	N/A
EP4 floxed x UBC-CreERT2	This study	N/A
EP2/4 double floxed x UBC-CreERT2	This study	N/A
Foxp3-DTR/EGFP	Jackson Lab	Cat# 016958
Oligonucleotides		
Primers for qRT-PCR	This paper	N/A
Software and algorithms		
FastQC v0.11.	Andrews, 2010	https://github.com/sandrews/FastQC
Prism	GraphPad	https://www.graphpad.com/scientific-software/prism/
ImageJ	NIH	https://imagej.nih.gov/ij/
Flowjo	BD Biosciences	https://www.flowjo.com/
LEGENDplex data analysis software suite	Biolegend	https://www.biolegend.com/ja-jp/legendplex/software
Cell Ranger (v3.1)	10x Genomics	https://support.10xgenomics.com/single-cell-gene-expression/software/downloads/latest
R Software	R Project	v3.6
Seurat	https://satijalab.org/seurat/index.html	v3.2.2
Celda	https://www.bioconductor.org/packages/release/bioc/html/celda.html	v1.2.4
clusterProfiler	https://bioconductor.org/packages/release/bioc/html/clusterProfiler.html	v3.14.3
biomaRt	https://bioconductor.org/packages/release/bioc/html/biomaRt.html	v2.42.1

RESOURCE AVAILABILITY

Lead contact

Requests for resources and reagents should be directed to and will be fulfilled by the lead contact, Shuh Narumiya (snaru@mfour.med.kyoto-u.ac.jp).

Materials availability

All unique reagents/mice generated in this study are available from the Lead contact with a completed Material Transfer Agreement.

Data and code availability

- scRNA-seq data have been deposited at GEO and are publicly available as of the date of publication. Accession number is listed in the Key resources table. Raw quantification data and original gross and microscopy images have been deposited at Mendeley and are publicly available as of the date of publication. The DOI is listed in the Key resources table.
- All computer codes used for the analyses have been deposited at GitHub and are publicly available as of the date of publication. The GitHub link is listed in the Key resources table.
- Any additional information required to reanalyze the data reported in this paper is available from the Lead contact upon request.

EXPERIMENTAL MODEL AND SUBJECT DETAILS

Tumor cell line

Lewis lung carcinoma cell line LLC1 (ATCC, CRL1642) was maintained at 37°C in 5% CO_2 in DMEM (Invitrogen), 10% FCS (Sigma), Pen/Strep (Nacalai) and Glutamine (Gibco).

Animal model

C57BL/6N mice (male or female, 6 weeks old) were purchased from SLC (Shizuoka, Japan) and kept under specific pathogen-free conditions. Genetic engineered mice used in this study were as listed in the "Experimental model: mice" sections of the Key resources table and kept similarly under specific pathogen-free conditions. All mice used in this study were bred to a C57BL/6N genetic background. Animal experiments were conducted in accordance with the US National Institutes of Health Guide for the Care and Use of Laboratory Animals and approved by the Institutional Animal Care and Use Committee of Kyoto University Graduate School of Medicine.

No human experiments were conducted within this study. However, clinical data that were previously reported and deposited at public available domain were used.

METHOD DETAILS

Synthesis of AS3385282-00

4 M HCl in dioxane (636 mL) was added to a solution of 1-*tert*-Butyl 4-ethyl 4-(iodomethyl)piperidine-1,4-dicarboxylate (compound 1) (Becker et al., 2005) (101 g, 254 mmol) in ethanol (450 mL). After stirring at 30°C for 2 h, the reaction mixture was concentrated under reduced pressure to give Ethyl 4-(iodomethyl)piperidine-4-carboxylate hydrochloride (compound 2) (75.0 g, 88%) as a gray solid.

Triethylamine (77.9 mL, 562 mmol) and 4-fluorobenzoyl chloride (37.4 g, 236 mmol) were then added to a suspension of compound 2 (75.0 g, 225 mmol) in THF (500 mL) at 0°C. The reaction mixture was stirred at 20°C for 3 h. Ethyl acetate (800 mL) and 1 M HCl (600 mL) were then added into the reaction mixture. The organic layer was separated and washed with brine, dried over Na_2SO_4, and concentrated under reduced pressure. The residue was purified by column chromatography on silica gel (petroleum ether/ethyl acetate = 10:1 to 2:1) to give Ethyl 1-(4-fluorobenzoyl)-4-(iodomethyl)piperidine-4-carboxylate (compound 3) (74.0 g, 78% yield) as a yellow oil.

4-(5-Chloropyrimidin-2-yl)phenol (Yuan et al., 2020) (36.5 g, 177 mmol) and K_2CO_3 (48.8 g, 353 mmol) were added at 20°C to a solution of compound 3 (74.0 g, 177 mmol) in dimethylacetoamide (400 mL). The reaction mixture was stirred at 130°C for 5 h. Ethyl acetate (1000 mL) and water (500 mL) were then added to the reaction mixture and the resulting mixture was filtered. The filtrate was separated and the organic layer was successively washed with water (500 mL x 5) and brine (1000 mL). The organic layer was dried over Na_2SO_4, and concentrated under reduced pressure to give a light yellow solid. The solid was triturated with petroleum ether/ethyl acetate (600 mL/80 mL) to give Ethyl 4-{[4-(5-chloropyrimidin-2-yl)phenoxy]methyl}-1-(4-fluorobenzoyl)piperidine-4-carboxylate (compound 4) (48.0 g, 55%) as a white solid.

Finally, 2 M NaOH aqueous solution (59.7 mL, 119 mmol) was added to a suspension of compound 4 (29.7 g, 59.7 mmol) in ethanol (300 mL) at 20°C. The reaction mixture was stirred at 75°C for 2 h. Water (1000 mL) and 1 M HCl (200 mL) were added into the reaction mixture, and the precipitate was filtered to give 4-{[4-(5-chloropyrimidin-2-yl)phenoxy]methyl}-1-(4-fluorobenzoyl)piperidine-4-carboxylic acid (AS3385282-00) (26.8 g, 96%) as a white solid.

Measurement of NMR and mass spectra of AS3385282-00

^{1}H NMR spectra was measured using Bruker Avance III 500HD spectrometer. Chemical shifts are expressed in δ units (ppm) using tetramethylsilane as an internal standard. Abbreviations of ^{1}H NMR signal patterns are as follows: s, singlet; d, doublet; t, triplet; m, multiplet; br, broad. Mass spectra (MS) were recorded on Waters SQD. Electrospray ionization positive high-resolution mass spectrum (HRMS) was performed using Thermo Fisher Scientific Exactive Plus.

For AS3385282-00; ^{1}H NMR (DMSO-d_6) δ 12.81 (br, 1H), 8.94 (s, 2H), 8.30 (d, J = 9.0 Hz, 2H), 7.51 – 7.45 (m, 2H), 7.27 (t, J = 9.0 Hz, 2H), 7.08 (d, J = 9.0 Hz, 2H), 4.16 (s, 2H), 3.64 – 3.05 (m, 4H), 2.24 – 1.95 (m, 2H), 1.76 – 1.51 (m, 2H) ppm; MS (ESI-) *m/z* 468.1 $[M-H]^-$; HRMS (ESI-) *m/z* Calcd for $C_{24}H_{20}ClFN_3O_4$ ($[M-H]^-$): 468.1121, Found: 468.1130.

cAMP assay

HEK293 cells overexpressing human EP2 or EP4 were seeded at 1×10^4 cells/ well in 96 well plates and incubated overnight. CHO-K1 cells overexpressing rat EP2 were seeded at 2×10^4 cells/well in 96 well plates and incubated overnight. Culture media was replaced first with Assay buffer (DMEM containing 2 μM indomethacin) for 1 hour. Cells were then incubated with IBMX buffer (Assay buffer containing 0.1 mM IBMX) for 5 min. AS3385282-00 was dissolved in dimethyl sulfoxide (DMSO) and diluted to a working concentration with IBMX buffer. After 10 min pretreatment with vehicle (0.1% DMSO) or AS3385282-00, HEK293 cells overexpressing human EP2 were stimulated by adding 30 nM PGE_2, HEK293 cells overexpressing human EP4 were stimulated by adding 10 nM PGE_2 and CHO-K1 cells overexpressing rat EP2 were stimulated by adding 300 nM PGE_2 for 30 min and lysed with lysis buffer (0.2% Triton X-100 in PBS). cAMP concentration in cell lysates was examined in duplicate using a cAMP-Gs Femto2 kit (Cisbio Bioassays, France) according to the manufacturer's instructions. Fluorescent signal was measured using a homogeneous time-resolved fluorescent plate reader Artemis (Furuno, Japan). The value of positive control (vehicle with PGE_2) was set as 0% inhibition, and the value of negative control (vehicle without PGE_2) was set as 100 % inhibition. IC_{50} values were estimated by nonlinear regression analysis using GraphPad Prism software.

Effect of AS3385282-00 on EP2 agonist-mediated blood pressure elevation in mouse

C57BL/6N mice (male, 7 weeks old) were used. Vehicle or AS3385282-00 (30, 100 or 300 mg/kg) were orally administered at 0 min. EP2 agonist (compound #936 of patent WO2009113600) dissolved in 3% PEG#400 containing 1.2 mM NaOH were intravenously administered at 0.3 mg/kg 10 min before blood pressure measurement. Six hours after vehicle or AS3385282-00 administration, the blood pressure (systolic blood pressure (SBP), diastolic blood pressure (DBP) and mean blood pressure (MBP)) were monitored using a tail cuff plethysmography (BP-98A-L, Softron, Japan) without any anesthesia and its value was calculated as a mean of three measurements. Group composition was as the following; (1) vehicle (n = 4), (2) vehicle + EP2 agonist (0.3 mg/kg) (n = 4), (3) AS3385282-00 (30 mg/kg) + EP2 agonist (0.3 mg/kg) (n = 4), (4) AS3385282-00 (100 mg/kg) + EP2 agonist (0.3 mg/kg) (n = 4), (5) AS3385282-00 (300 mg/kg) + EP2 agonist (0.3 mg/kg) (n = 3).

Cell viability assay

Cell viability *in vitro* was measured by CellTiter-Glo® 2.0 Cell Viability Assay kit (Promega). For each assay, 100 μL cell suspensions (2×10^5 cells/mL) were cultured in 96-cell plates for 24 h and then treated with AS3385282-00 or ASP7657 or AS3385282-00 in combination with ASP7657 for 48 h. Luminescence was then measured by GLOMAX Multi + Detection System (Promega) after incubation for 10 min with CellTiter-Glo 2.0 reagent according to manufacturer's protocol. The vehicle-treated cells, incubated in culture medium containing 0.5% dimethylsulfoxide (DMSO), were used as controls in every test. Results were presented as a percentage of the vehicle-treated control cells.

Tumor cell injections and tumor growth experiments

For LLC1 tumor cell injection, floating cells were first collected from the supernatant and then the adherent tumor cells were collected by rigorously pipetting and washed 2 times with DPBS. These cells were mixed together and resuspended in DPBS at the concentration of 3×10^5 cells/100 μL. Mice anesthetized with isoflurane were shaved on their right flank and injected with 100 μL suspension of the tumor cells. Tumors were measured using electronic calipers. Tumor volume was calculated through the formula V = (long diameter) x $(\text{short diameter})^2$ x 1/2 (mm^3).

Mouse tumor tissue digestion

Tumor tissues were dissected and enzymatically digested with the mouse tumor dissociation kit (Miltenyi) and gentleMACS C tube (Miltenyi), and the digests were subjected to agitation and rotation at 37°C for 30 min according the manufacturer's protocol. Red blood cells were lysed with red blood cell lysis solution (Miltenyi). Cell suspensions were then filtered through a 70 μm filter (Miltenyi) and washed with FACS buffer containing 1% BSA (Sigma).

Single-cell RNA sequencing (scRNA-seq)

For scRNA-seq experiment of EP2/4 antagonists-treated mice (both 6-days and 1.5-days treatment), live $CD45^+$ cells were sorted from dissected LLC1 tumor cell suspension using BD Aria3 FACS sorter (BD Biosciences). For scRNA-seq experiment of Treg-depleted mice, total cells from the dissected LLC1 tumor were used. Single-cell isolation and library preparation were performed using Chromium™ Next GEM single cell 3' GEM, library & gel bead kit v3.1, i7 multiplex kit and Next GEM Chip G single cell kit according to the manufacturer's protocol (10x Genomics). For human LUSC scRNA-seq, data were obtained from publicly available domain (Maier et al., 2020).

Single-cell data processing

Single-cell RNA-seq libraries were sequenced on Illumina NovaSeq 6000 sequencer to a depth of ~60,000 reads/target cells. The qualities of raw sequencing reads were then evaluated with FASTQC (http://www.bioinformatics.babraham.ac.uk/projects/fastqc/) and aligned using the Cell Ranger Software v3.1 (10x Genomics, USA) against the mm10 mouse genome reference. Ambient mRNA reads were predicted and removed by *decontX* command under the celda package (Yang et al., 2020).

Quality control, cellular identification and clustering analysis

For each sample, the ambient mRNA removed gene – barcode matrix was further processed by the R (v3.6) software package Seurat (Stuart et al., 2019) (https://satijalab.org/seurat) (v3.2.2) for all downstream analyses. We then filtered on cells that expressed a minimum of 1500 UMI count and required that all genes expressed in a cell be expressed in at least 3 cells. We also removed cells that contained >10% mitochondria gene reads, which is thought to be associated with unhealthy cells. SC transform normalization (Hafemeister and Satija, 2019) were used for batch correction and integration into a single dataset. Principal component (PC) analysis was performed and then used for graph-based cluster identification and subsequent dimensional reduction using Uniform Manifold Approximation and Projection (UMAP). Count data was then normalized using NormalizeData by Seurat package for expression study and differential analysis. Functional enrichment analysis was performed using the clusterProfiler package (Yu et al., 2012), biomaRt (v.2.42.1) and org.Mm.eg.db (v3.10.0) mouse genome annotation. For each cell population, we performed DE analysis by comparing two conditions, drug treatment versus control vehicle using command *FindMarkers.*

FACS analysis

Single cell suspension of tumor tissues was washed with PBS and stained with fixable viability dye (eBioscience) or violet fluorescent reactive dye (Invitrogen) for 30 min at 4°C to distinguish live and dead cells. Cells were then washed with FACS buffer and non-specific-binding was blocked with anti-CD16/32 antibodies (Fc block, BD Biosciences). Cell surface proteins were then stained on ice for 30 min. Cells were washed again and re-suspended with FACS buffer. FACS analyses were conducted using BD Fortessa, BD Aria3 or BD Fusion flow cytometer (BD Biosciences). For intracellular staining (Foxp3 or Gzmb), cells were fixed and permeabilized with the Foxp3/Transcription Factor Staining Buffer kit (eBioscience) after surface markers staining. Intracellular antibody staining was performed in permeabilization buffer for 30 min at room temperature. FACS data analysis was performed using FlowJo software (BD Biosciences).

The definition of each cell population from *in vivo* tumor is as follows;
$CD45^+$ cells: FVD^-CD45^+;
$CD45^-$ cells: FVD^-CD45^-;
CD4 T cells: $FVD^-CD45^+CD11b^-CD3^+CD4^+$;
CD8 T cells: $FVD^-CD45^+CD11b^-CD3^+CD8^+$;
$Gzmb^+$ CD4 T cells: $FVD^-CD45^+CD11b^-CD3^+CD4^+Gzmb^+$;
$Gzmb^+$ CD8 T cells: $FVD^-CD45^+CD11b^-CD3^+CD8^+Gzmb^+$;
Treg: $FVD^-CD45^+CD3^+CD4^+CD25^{hi}Foxp3^+$
4-1BB$^+$Treg: $FVD^-CD45^+CD3^+CD4^+CD25^{hi}Foxp3^+$4-1BB$^+$
Mono: $FVD^-CD45^+CD11b^+F4/80^-Ly6C^{hi}Ly6G^-$;
TAN: $FVD^-CD45^+CD11b^+F4/80^-Ly6C^{lo}Ly6G^+$;
TAM: $FVD^-CD45^+CD11b^+F4/80^+Ly6C^-Ly6G^-$;
NK: $FVD^-CD45^+CD3^-NKp46^+$;
$Ccr7^+$ cDC: $FVD^-CD45^+lin^-(CD3^-NK1.1^-F4/80^-Ly6C^-Ly6G^-)$I-A/I-E$^+$ $CD11c^+CD11b^{+/-}Ccr7^+$;
cDC1: $FVD^-CD45^+lin^-(CD3^-NK1.1^-F4/80^-Ly6C^-Ly6G^-)$I-A/I-E$^+$ $CD11c^+CD11b^-$ $Ccr7^-$;
cDC2: $FVD^-CD45^+lin^-(CD3^-NK1.1^-F4/80^-Ly6C^-Ly6G^-)$I-A/I-E$^+CD11c^+CD11b^+Ccr7^-$
iTreg cells in *in vitro* experiments are defined as follows;
iTreg: $CD4^+CD25^{hi}Foxp3^+$ in the iTreg stability assay or $CD4^+Foxp3^+$ in the 4-1bb induction assay.
4-1bb$^+$ iTreg: $CD4^+Foxp3^+$4-1bb$^+$

ELISA assay for Ccl22 and Ccl17 measurement in sort-purified $Ccr7^+$ cDC, cDC2, CD45(−) cell and TAM from LLC1 tumor

Live $Ccr7^+$ cDC, cDC2, CD45(−) cell and TAM were sorted from the dissected LLC1 tumor using BD Aria3 FACS sorter (BD Biosciences). Sorted cells were subsequently washed with PBS and the cultured in complete RPMI (Pen/Strep, NEAA, NaPyr, 2-ME, 10% FCS) in 96-well plates at 2×10^5 cells/200 μL/well. LPS (1 μg/mL, Nacalai) were added after plating to stimulate chemokine production of the cells. Culture supernatants were collected 36 hours after stimulation and Ccl22 and Ccl17 production were measured by the used of LEGENDplex (Biolegend) and BD Fortessa flow cytometer (BD Biosciences) according to the manufacturer's instruction. Data analysis were conducted by the use of LEGENDplex data analysis software suite.

Treg *in vitro* culture assays

For induction of iTreg, MACS (Miltenyi)-purified splenic naïve CD4 T cells were stimulated with plate-bound anti-CD3 mAb (clone 2C11, eBioscience) (coating at 10 μg/mL for overnight at 4°C) and 1μg/mL soluble anti-CD28 mAb (clone 35.71, eBioscience) in the presence of 5 ng/mL of human TGF-β1 (R&D), in 96-well U bottom plates (Thermo scientific, 163320). For iTreg stability assay, iTreg prepared by culture in the presence of TGF-β1 for 2 days as above were collected, washed once, and further cultured at 1×10^6/ml concentration with fresh RPMI culture medium containing 10% FBS (Gibco) and 50 U/mL of IL-2 (Prepotech). PGE_2 (Cayman) were added in the second culture. An EP2 antagonist (PF 04418948, Tocris) and an EP4 antagonist (ASP7657, Astellas) were added to the cells 30 min before the addition of PGE_2. For analysis of the role of PGE_2 on the differentiation of iTregs from

MACS purified splenic naïve CD4 T cells, cells were cultured in fresh RPMI culture medium containing 10% bovine serum (Gibco) and 5 ng/mL of human TGF-β1 (R&D) in the presence of PGE_2.

Quantitative RT-PCR analysis

Live TAN, Mono, TAM, $CD45^+$ cells and $CD45^-$ cells were sorted from the single cell suspension of LLC1 tumor using BD Aria3 or BD Fusion FACS sorter (BD Biosciences). mRNA was extracted from TAN, Mono and TAM using RNeasy Plus Micro kit (Qiagen) and reverse-transcribed to cDNA using ReverTra Ace qPCR RT master mix with gDNA Remover (Toyobo). mRNA was extracted from sort-purified $CD45^+$ and $CD45^-$ cells using TRIzol (Ambion) and conventional chloroform/isopropanol extraction protocol, washed with ethanol (Nacalai) and, reverse-transcribed to cDNA using ReverTra Ace qPCR RT master mix with gDNA Remover (Toyobo). cDNA, primers, and THUNDERBIRD SYBR qPCR Mix (Toyobo) were mixed in a 96-well PCR plate. Subsequently, quantitative PCR (qPCR) was performed using a CFX96 Real-Time System (Bio-Rad). The sequences of primers are listed in Table S6.

Drug administration and anti-PD-1 antibody treatment

SC-560 (Cox1 inhibitor) was purchased from TCI, and dissolved with PEG#600 (Nacalai) every day before use. The solution was orally administered after mice were transplanted with LLC1 tumor cells at the dose of 30 mg/kg/day for every day. Celecoxib (Cox2 inhibitor) was purchased from Cayman. Celecoxib was dissolved with PEG#400 (Nacalai) and then normal saline (Otsuka) at the volume ratio of 3:1 before use every day. The solution was orally administered after mice were transplanted with LLC1 tumor cells at the dose of 30 mg/kg/day for every day. For SC-560 and Celecoxib treatment in combination, the respective solution was orally administered at the dose of 30 mg/kg/day daily.

For treatment with anti-PD-1 monoclonal antibody (clone RMP1-14, BioXCell) was administered i.p. at the dose of 200 μg/mouse from day 3 post-tumor cell transplantation every 3 to 4 days. Rat IgG2a (clone 2A3, BioXCell) was used as isotype control.

For EP2 antagonist (AS3385282-00, this study), the drug was dissolved in PG solvent (Tween 80:HCO-40:PG at 1:2:4 weight ratio) at 80°C with sonication. 1M sodium hydrogen carbonate, 50% HP-βCD and HCl were then further added and rigorously mixed to obtain a final solution of AS3385282-00 containing 60%PG solvent: 8.5% 1M sodium hydrogen carbonate: 7% HP-βCD: 2% 1M HCl in distilled water (Otsuka). Drug was prepared once a week and kept in dark at room temperature. Mice were orally administered once daily with AS3385285-00 at the dose of 100 mg/kg/day.

For EP4 antagonist, ASP7657 (Astellas), the drug was suspended every 3–4 days in 0.5% methylcellulose (Wako chemical) solution with sonication and kept in dark at 4°C. Mice were orally administered twice daily with ASP7657 at the dose of 1 or 10 mg/kg/day.

For tamoxifen-induced EP4 cKO and EP2/4 cDKO experiments, tamoxifen (Sigma) was intraperitoneally injected into EP2/4 floxed mice (as control), EP4 floxed x UBC-creERT2 mice or EP2/4 double-floxed × UBC-creERT2 mice at a dose of 3.2 mg/day for 5 consecutive days. Subsequently, 5 days after last tamoxifen injection, peripheral blood (tail vein) were sampled. Peripheral blood mononuclear cells were isolated according to standard protocol and then subjected to RNA extraction and qRT-PCR analysis for *Ptger2* and *Ptger4*. Mice with knockout efficiency more than 50% were selected for LLC1 tumor cell transplantation.

Treg depletion and depletion of CD8 T cells

For Treg depletion, mice were intraperitoneally injected with 1 μg of diphtheria toxin (DT, Sigma). Foxp3-DTR/EGFP mice were injected on when tumor size reached 20∼30 mm^3 (usually day 10-11) and thereafter every 3–4 days. For CD8 T cells depletion in WT mice treated with vehicle or EP2 KO mice treated EP4 antagonists, IgG2b isotype (Clone: LTF-2, BioXCell) or anti-CD8a antibody (Clone: 2.43, BioXCell) were injected intraperitoneally at days −1, 0, 3 at the dose of 100 μg, and thereafter at days 7 and 14 at the dose of 200 μg.

Ccl17 and Ccl22 neutralization

For Ccl17 and Ccl22 neutralization *in vivo*, anti-Ccl17 antibody and anti-Ccl22 antibody (goat anti-mouse antibodies; R&D Systems) were administered i.p. at 20 μg/mouse on alternate days starting from day 10 after tumor transplantation. Normal goat IgG (R&D) was used as isotype control.

Histology and immunohistochemistry

Tumors were dissected and fixed in 10% formalin neutral buffer solution (FUJIFILM Wako Pure Chemical) at room temperature. Fixed tumor tissues were then embedded in paraffin and cut into sections at 2 μm thickness. Hematoxylin and eosin staining was performed using a standard protocol. For immunohistochemistry, paraffin sections were incubated with target retrieval solution (Dako, S2367), pH 9 at 110°C for 15 min for antigen retrieval and then treated with 3% H_2O_2 for 5 min to quench endogenous peroxidase activity, followed by blocking with 3% goat serum in PBS for 20 min. The sections were subsequently incubated with anti-CD31 antibody diluted at 1:600 (Abcam), for overnight at 4°C, then Dako EnVision+ System-HRP labelled polymer, anti-rabbit IgG (Dako). The HRP activity was finally detected by liquid DAB^+ substrate chromogen system (Dako). Bright field images were acquired with Nanozoomer-XR system (Hamamatsu Photonics) equipped with UPlanFI 20×/0.75 microscope objective lens and a CCD camera. Images were processed using NDP view 2 (Hamamatsu Photonics) and analyzed with ImageJ (NIH).

Bioinformatics analysis of TCGA database

The TCGA gene expression and survival datasets were obtained from UCSC Xena datapages (https://xenabrowser.net/datapages/). Heatmaps showing correlation between gene expression were produced using the ggplot2 package (v3.3.3) (Wickham, 2009). Kaplan-Meier plots for overall survival for 5 years were generated and the expression levels of PTGER2, PTGER4 or both PTGER2 and PTGER4 were stratified with 2 different cut-offs: 25% and 75% to segregate the patients. The comparison that was statistically significant are shown. All survival analysis was carried out and plotted using the R survival (v2.44.1.1) and survminer (v0.4.9) packages.

QUANTIFICATION AND STATISTICAL ANALYSIS

Quantitative analysis of blood vessels density

The image of CD31 immunohistochemistry contains brown $CD31^+$ blood vessels endothelial cell signals and the blue Hematoxylin counter-staining. To separate these two structures and analyze the area of blood vessels, the blue and purple saturation of nucleus was reduced to enhance $CD31^+$ blood vessels clarity. The blood vessels were then enhanced to highlight the blood vessels structure and the area was then measured using ImageJ (NIH) and Vessel Analysis plugin (developed by Govindaraju and Elfarnawany). Subsequently, another image of the Hematoxylin counter-staining was used for the measurement of total area of tumor. The blood vessel occupancy was then computed as the ratio between the area of blood vessels and the total area of tumor.

Statistical analyses

Excel (Microsoft, USA) and Prism (GraphPad Software, USA) were used for statistical analyses. Data (means ± standard error of the mean (SEM)) or (means ± standard deviation (SD)) were analyzed either by using Student *t*-test (two-tailed), one-way Analysis Of Variance (ANOVA) followed by Tukey's correction for multiple testing or Dunnett's test compared to the control or, two-way Analysis Of Variance (ANOVA) followed by Tukey's correction for multiple testing or Dunnett's test compared to the control or Bonferroni's test. R software (R Core Team, 2014) was used for statistical analysis of scRNA-seq datasets and TCGA datasets. Differential expression gene analysis was done by command FindMarkers in Seurat Package and Wilcoxon Rank Sum test was calculated. Survival analysis was done by command ggsurvplot in Survminer Package and LogRank test was calculated. Gene expression correlation analysis in TCGA dataset was done by command cor.test in Stat package and, pairwise Pearson correlation coefficients and $-\log_{10}$ p values were computed.